Finite Element Analysis of Stress States in Patient-Specific Intraluminal Thrombi and Walls of Abdominal Aortic Aneurysms: The Influence of Residual Stresses

A thesis in partial fulfillment
of the requirements to achieve the academic degree
Master of Science

submitted to the
Faculty of Mechanical Engineering and Economic Sciences
at Graz University of Technology

by

Thomas E Fastl, BSc

Supervisors: David M Pierce, PhD
Professor Gerhard A Holzapfel, PhD

April 4, 2013

STATUTORY DECLARATION

I declare that I have authored this thesis independently, that I have not used other than the declared sources/resources, and that I have explicitly marked all material which has been quoted either literally or by content from the used sources.

Graz, _____   _____
               Date   Signature

EIDESSTATTLICHE ERKLÄRUNG

Ich erkläre an Eides statt, dass ich die vorliegende Arbeit selbstständig verfasst, andere als die angegebenen Quellen/Hilfsmittel nicht benutzt, und die den benutzten Quellen wörtlich und inhaltlich entnommenen Stellen als solche kenntlich gemacht habe.

Graz, am _____   _____
               Datum   Unterschrift

Abstract

Numerical modeling in biomechanics and mechanobiology has grown in popularity over the last few decades and provides a powerful method to calculate clinically relevant *in vivo* parameters for physiological as well as pathopysiological conditions. In particular, patient-specific finite element models may improve early detection and guide clinicians in subsequent treatment. Moreover, numerical simulation can be applied to better predict certain catastrophic events such as rupture of abdominal aortic aneurysms via assessment of rupture potential. Hence, there is an increasing demand on numerical simulations from clinicians and society.

Recent progress in medical imaging, image analysis, and finite element meshing tools allows to extract detailed patient-specific geometries of anatomical structures, e.g., abdominal aortic aneurysms, and thus facilitates solving clinical problems by using the finite element method. Due to diagnostic *in vivo* imaging the reconstructed computer geometry represents a configuration under specific boundary conditions such as physiological blood pressure. Classical continuum mechanics including related material models and the corresponding finite element implementation are based on an unloaded and stress-free reference configuration. As a consequence, two problems arise from the application of such classical approaches to patient-specific models of abdominal aortic aneurysms: (i) the imaged and subsequently reconstructed 'initial' geometry is subjected to *in vivo* boundary conditions, and (ii) residual stresses are known to exist in the unloaded human arterial tissue, which significantly influence the overall stress distribution within the arterial wall.

Computational algorithms for prestressing the arterial reference configuration have been presented to address the first problem. However, the second problem, that of *in vivo* residual stresses in patient-specific finite element simulations, has still not been satisfactorily addressed in the literature. Therefore, a pragmatic approach to incorporate experimentally-determined three-dimensional residual stresses (stretches) in patient-specific finite element simulations of abdominal aortic aneurysms including the layered structure (intima, media, adventitia) of the arterial wall is described. A novel approach to calculate the local directions of anisotropy related to constitutive material modeling applicable for structured and unstructured finite element meshes is also presented.

Systematic numerical analysis indicates that the proposed method is, in general, applicable to arterial tissues and abdominal aortic aneurysms. A decrease in circumferential stress for the intima and an increase in the media and the adventitia are observed, which tends to homogenize the stress distribution within the arterial wall. However, high variations of stresses are found in the circumferential direction in all layers, indicating that the spatial variation of three-dimensional residual stresses as well as related passive material parameters need to be investigated in more detail. This may lead to more uniformity of circumferential stresses, which has been hypothesized and reported in the biomechanics literature.

Zusammenfassung

Die numerische Modellierung im Bereich der Biomechanik und Mechanobiologie hat in den vergangenen Jahrzehnten stark an Popularität gewonnen und bietet eine Methode, um medizinisch relevante *in vivo* Parameter im physiologischen, aber auch im pathophysiologischen Zustand zu berechnen. Patientenspezifische Finite-Elemente-Modelle haben das Potential, eine Früherkennung zu erleichtern und Ärzten bei Entscheidungen über die Behandlung zu unterstützen. Numerische Simulationen können weiters für die Vorhersage von lebensbedrohlichen Gegebenheiten, z.B. der Ruptur eines Aneurysmas der abdominalen Aorta durch Einschätzung des Rupturpotentials, angewandt werden. Daraus resultiert eine steigende Nachfrage an numerischen Berechnungen von Ärzten und Gesellschaft.

Neueste Fortschritte in medizinischer Bildgebung, Bildanalyse und Finite-Elemente-Netzgenerierung erlauben eine detailierte Rekonstruktion von patientenspezifischen anatomischen Strukturen, wie einem abdominalen Aortenaneurysma. Dadurch ergibt sich die Möglichkeit, klinisch relevante Problemstellungen mit der Finite-Elemente-Methode zu lösen. Aufgrund der diagnostischen *in vivo* Bildaufnahme repräsentiert die rekonstruierte Computergeometrie eine Struktur unter Einfluss von physiologischen Randbedingungen wie dem Blutdruck. Die klassische Kontinuumsmechanik, die damit verbundenen Materialmodelle sowie auch die Implementierung in Finite-Elemente-Programmen basieren auf der Annahme einer spannungs- und belastungsfreien Referenzkonfiguration. Die Anwendung dieser klassischen Ansätze auf Simulationen von abdominalen Aortenaneurysmen führt zu zwei grundlegenden Problemen: (i) Die aufgenommene und rekonstruierte Geometrie der anatomischen Struktur steht unter Einfluss von *in vivo* Randbedingungen und (ii) arterielles Gewebe beinhaltet ohne jegliche Lastaufbringung Eigenspannungen, welche die Spannungsverteilung in der Arterienwand signifikant beeinflussen.

Das Aufbringen von *in vivo* Randbedingungen bei gleichzeitigem Beibehalten der Referenzkonfiguration wurde bereits mit verschiedenen Computeralgorithmen gelöst, wogegen das Einbeziehen der Eigenspannungen in patientenspezifische Finite-Elemente-Simulationen nur unzureichend behandelt wurde. Aus diesem Grund wird eine pragmatische Herangehensweise vorgestellt, bei welcher die dreidimensionalen Eigenspannungen (Eigendehnungen) in patientenspezifische Finite-Elemente-Simulationen von abdominalen Aortenaneurysmen unter Berücksichtigung der Schichtstruktur (Intima, Media, Adventitia) inkludiert werden. Zusätzlich wird ein neuer Ansatz zur Berechnung von lokalen Vorzugsrichtungen, welche für anisotrope Materialmodelle von großer Bedeutung sind, präsentiert.

Die systematisch durchgeführte numerische Analyse zeigt, dass die Methode generell für Arterien und abdominale Aortenaneurysmen angewendet werden kann. Eine Verminderung der Umfangsspannung in der Intima bei gleichzeitiger Erhöhung in Media und Adventitia tendieren zu einer homogeneren Verteilung. Hohe Spannungsschwankungen entlang der Arterienwand in den individuellen Schichten weisen darauf hin, dass möglicherweise

lokale Unterschiede in der dreidimensionalen Eigenspannungsverteilung und den passiven Materialparametern vorliegen. Das Einbeziehen dieser Unterschiede in die numerischen Simulationen könnte zu einer weiteren Homogenisierung der Spannungen beitragen, was in der Biomechanikliteratur vermutet wird.

Preface

This thesis was motivated by and performed in collaboration with the research project 'SCATh: Smart Catheterization Towards Sustainable and Personalized Healthcare' with the European Commission (Call ID: FP7-ICT-2009-4, Objective: ICT-4-5.2) as the awarding agency at the Institute of Biomechanics at Graz University of Technology, Austria. This support is gratefully acknowledged.

I would like to express my genuine and deep gratitude to David M Pierce, Phd for his excellent supervision, sustained patience, and endless support during the conduction of this work. I also want to express my sincere gratitude to Professor Gerhard A Holzapfel, Phd for ample valuable discussion, advice, and assistance as well as for the introduction to the fascinating field of biomechanics. Especially, I would like to thank both of you for giving me the opportunity to work in this exciting scientific field and for introducing me to the scientific community through international conferences, summer schools, and symposia.

I am particularly in debt and want to take the opportunity to thank a very special person, Thomas SE Eriksson, PhD, a former coworker of mine, who subsequently became one of my closest friends and guided me in many difficult situations over the past several years. Thank you so much for your scientific criticism, brilliant advice, as well as for the social competence you communicated to me.

Furthermore, I want to thank all my colleagues at and affiliates of the Institute of Biomechanics at Graz University of Technology for the opportunity to work in a such positive and stimulating environment. It was really a pleasure for me to be a part of this research group as a teaching assistant and master student.

In addition, I also want to direct many thanks to numerous friends and student colleagues, who supported me in their individual ways in various situations throughout years at Graz University of Technology and tolerated my absence during performance of this work.

Finally, I want to thank the most important persons in my life, my mother Anna M and my father Erhard J Fastl, for all their encouragement, patience, and support in financial and social matters they have given since my childhood, as well as my sister Marlies A Fastl, who always had a sympathetic ear for my concerns.

<div align="right">

Thomas E Fastl
Graz, April 4, 2013

</div>

CONTENTS

1 INTRODUCTION AND MOTIVATION

1.1 Modeling in Biomechanics

The world health organization (WHO) has identified cardiovascular disease (CVD) as the leading cause of death worldwide, affecting every third person of the global population. This already frightening fact is accompanied with a continuous increase in total fatalities per year in the near future. In the United States of America, for example, CVD accounts for 32.8% of all deaths, while the percentage in Europe (approximately 47%) is even higher [45, 55]. An abdominal aortic aneurysm (AAA) represents a specific type of CVD with a prevalence of 4-8.9% in older men and 0.5-2.2% in older women [14, 42]. In developed countries 1.3% of all deaths among older men are associated with AAA rupture [56], a catastrophic event, leading to death if immediate surgical intervention is not available. However, not all AAAs are suspected to instantly rupture since AAA formation may proceed over several years and might stabilize during evolution. Therefore, it is important to identify the potential of an individual AAA to rupture, i.e., to characterize its rupture risk. Societal expenses for medical diagnosis and conventional patient treatment including associated open surgery as well as emergency intervention of AAAs add up to a staggering amount due to the high prevalence of this particular disease. Improved identification, especially improved early detection, and the evaluation of the risk of rupture combined with adequate and adapted treatment procedures will lead to a decrease in health care costs and also, even more important, to a significant increase in patient's life quality. Hence, there is a real need for improved patient-specific finite element (FE) simulations of AAAs to gain additional insight into human physiology and pathophysiology, and obtain more reliable stress estimates to better characterize rupture risk.

Patient-specific AAA geometries are reconstructed from computer tomography angiography (CTA) or magnetic resonance imaging (MRI) scans, thus representing a deformed configuration subjected to physiological *in vivo* boundary conditions. The framework of classical continuum mechanics and related constitutive material models as well as the FE method itself are based on the definition of an unloaded and stress-free reference state. As a consequence, two problems arise from the application of such classical approaches to patient-specific FE simulations of AAAs: (i) the *in vivo* image derived geometry is not load free, and (ii) the unloaded arterial tissue is residually stressed. The first problem has been addressed by numerous computational algorithms (e.g., [19, 68]), whereas the inclusion of residual stresses in patient-specific FE simulations has not been satisfactorily solved in the biomechanics literature. In this thesis a consistent framework for incorporation of experimentally-determined residual stresses in patient-specific FE simulations of AAAs

is presented to improve prediction of stress states and enhance characterization of AAA rupture risk. The proposed method is, in general, applicable to any residually stressed soft biological tissue (e.g., arteries) where data on residual deformation are available.

1.2 Arterial Wall Mechanics

Fundamental stress analysis via the FE method of human arterial tissue requires constitutive material models representing the biological tissue in sufficient detail concerning the macroscopic as well as the underlying microscopic structure. Therefore, it is essential to investigate the morphology and the histology of individual arteries in healthy and diseased states. The identification of the constituents and their mechanical contribution to the overall material behavior leads to conclusions of their individual role within the considered artery. These medical and mechanical findings form the basis to develop adequate computer models of human arteries such as, e.g., the thoracic aorta, the abdominal aorta, the common iliac arteries, etc., and enable the prediction of stress up to a certain accuracy.

1.2.1 Healthy Human Arterial Wall

In general, human arteries can be divided into two types: (i) elastic arteries located close to the heart, and (ii) muscular arteries present in the periphery [31]. These two types of arteries accomplish different functions within the human body, nevertheless they share a common macroscopic structure in healthy conditions and are composed of three distinct layers, the intima, the media, and the adventitia (see Fig. 1.1). In the following, the constituents of the arterial wall, in particular of every individual layer, are discussed from a mechanical perspective describing their individual contribution in constitutive modeling issues.

Intima (tunica intima).   The intima (tunica intima) is the innermost layer of the artery consisting of a single layer of squamous longitudinally aligned endothelial cells covering the vessel wall and resting on a very thin basal lamina. This lamina separates the endothelial cells from the subendothelial layer, whose thickness and constituents change with age [52]. The intima is bordered by the internal elastic lamina, generally not considered as part of the intima and absent in geometrical transition zones such as, e.g., the bifurcation [60]. The subendothelial layer might be almost absent in young healthy individuals, resulting in a very thin intima having only minor contribution to the mechanical properties of arteries. This justifies the assumption to neglect the intima in FE simulations for young and healthy humans [24]. However, physiological adaption to mechanical stresses, known as arteriosclerosis, stiffens and thickens (eccentric or diffuse intimal thickening [60]) the intima in a significant manner, thus requiring to discard this assumption and introducing the necessity of modeling the intima [27].

In contrast to arteriosclerosis, which is a physiological aging process, the term atherosclerosis refers to a systemic, lipid-driven inflammatory disease associated with multi-focal plaque development (atherosclerotic plaque) [71]. Beside hypertension, atherosclerosis
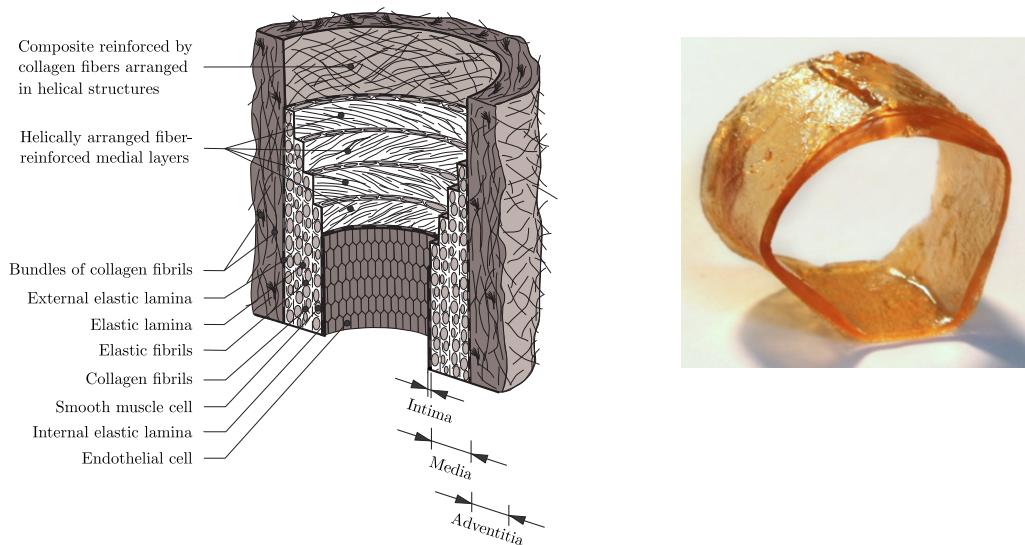
Figure 1.1: Schematic model of a healthy human artery illustrating the macroscopic structure of the three distinct layers intima, media, and adventitia and their major constituents adapted from [24] (left panel). Segment of a human abdominal aorta after an optical clearing process illustrating its translucent appearance [57] (right panel).

is known to be the most common CVD, which might also affect the media in more advanced stages, thereby significantly changing the overall mechanical behavior of the arterial wall.

Media (tunica media). From the mechanical perspective, the media (tunica media), representing the middle layer of an artery, is the most important and, in general, also the thickest layer in healthy human arteries. It makes a significant contribution to the overall strength of arterial tissue due to its highly structured and very complex three-dimensional arrangement of smooth muscle cells, elastic sheets (elastic laminae), collagen, and elastic fibrils. There are varying numbers (decreasing towards the periphery) of fenestrated elastic laminae separating the media into individual concentrically aligned sublayers interconnected via elastic fibrils [52]. Furthermore, it is assumed that the closely interconnected constituents of the media in connection with their orientation form a continuous fibrous helix (Faserschraube) with a small pitch, leading to an almost circumferential alignment of fibrils [24]. The internal elastic lamina and the external elastic lamina separate the media towards the intima and the adventitia, respectively.

Adventitia (tunica adventitia). The adventitia (tunica adventitia) is the outermost layer of the arterial wall mainly consisting of fibroblasts and fibrocytes (collagen and elastin production), histological ground substance (extracellular matrix), and elastic and thick interwoven collagen fibrils forming a fibrous tissue [24]. The adventitia itself grad-

ually merges with the loose surrounding connective tissue, which serves as a delineation towards other organs in the human body. In general, the thickness of the adventitia varies with the location in the human body and might become virtually absent for different types of arteries. The adventitia with constituting helically arranged and wavy (physiological diastolic load state) collagen fibrils seems to serve as a layer limiting the stretch, therefore preventing arterial rupture in high pressure regimes [58]. This hypothesis is substantiated by the observation of an exponential-like increase in stiffness due to collagen fiber recruitment and fiber stretch.

1.2.2 Abdominal Aortic Aneurysm

A focal, in general, asymmetric dilatation of the infrarenal aorta exceeding a maximum diameter of 3 cm (clinical characterization) is diagnosed as a AAA. Nevertheless, because of variations in aortic diameter depending on sex, age, bodyweight, and the position within the abdomen (diameter decreases towards the common iliac arteries) a new criterion was proposed so that a AAA is present if the current aortic diameter exceeds 150% of its initial one [56]. Characterization of AAAs can be also performed on a histological basis since AAA formation is associated with a loss of medial elastin and smooth muscle cells [12], as well as structural changes in the orientation and alignment of collagen fibers in the entire AAA wall (see Fig. 4.1). Risk factors for AAA formation can either be acquired as a consequence of, e.g., atherosclerosis, hypertension, or smoking, or inherited, e.g., Marfan syndrome or Ehlers-Danlos syndrome [29]. The shape of a AAA, more general its anatomy, can be described as being either fusiform or saccular. Saccular AAAs dilate the vessel only on one side, whereas fusiform AAAs, which are more common, bulge out at the hole circumference. The majority of AAA walls are covered by an intraluminal thrombus (ILT), a three-dimensional fibrin structure incorporating blood proteins, blood cells, platelets, and cellular debris [63]. In the ILT three individual layers can be identified suggesting that it is also a highly heterogeneous material.

As a consequence of the high mortality rate due to AAA rupture, surgeons have to decide in clinical practice if a particular patient needs AAA repair (see Fig. 1.2). This decision is based on the balance of the risk of rupture against the risk of elective repair. A widely accepted routine is to advocate clinical intervention if the maximum diameter of the lesion reaches 5.0 mm in women and 5.5 mm in men or if the maximal diameter increases more than 0.5-1.0 mm in one year [30]. Physically, the maximum diameter criterion is based on the Law of Laplace, a relationship assuming a cylindrical geometry with constant wall thickness and linear elastic material properties [51]. It is not surprising that smaller AAAs might rupture (e.g., 13% of AAAs smaller than 5 cm), whereas larger ones (e.g., 54% of AAAs larger than 7.1 cm) remain stable and do never rupture [66].

Mechanical perspective predicts lesion rupture if the peak wall stress exceeds the local wall strength. Therefore, a more sophisticated approach to identify the rupture risk of a AAA is the application of the nonlinear FE method, which enables modeling of complex three-dimensional geometries with varying wall thickness, associated boundary conditions, and
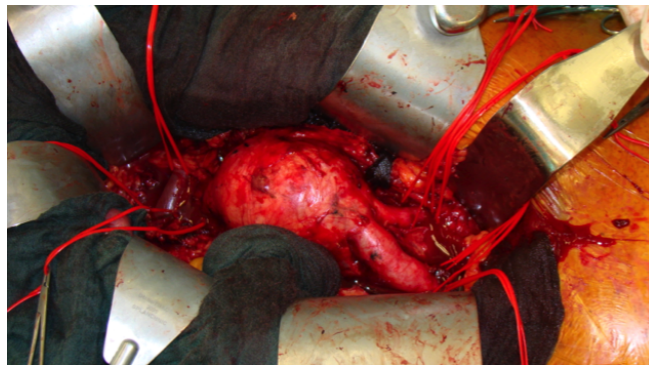
Figure 1.2: Surgical intervention of a representative AAA taken with permission from [51].

the nonlinear properties of the AAA wall. In addition to that, computational FE simulations can also take the influence of the ILT and possibly integrated calcifications and lipid pools into account [16, 28]. The reader is referred to [30] for an overview of continuously improving FE simulations of AAAs accounting for additional complexity in analysis. However, several inappropriate assumptions are still made within the biomechanics community, which might lead to subsequent incorrect findings (e.g., [53, 54]).

1.2.3 Residual Stresses/Stretches

In the 1960s it was reported that there exists '*some degree of stress even when there is no distending pressure*' in an artery [6]. To the authors knowledge, this was the first time presuming that arterial tissue is not stress-free in the unloaded configuration. Subsequent studies independently observed and confirmed the existence of residual stresses in arteries [15, 64]. These residual stresses have the potential to homogenize the stress distribution within the arterial wall in physiological load states. In fact, several studies have shown that the inclusion of residual stresses, even if they are small compared to *in vivo* wall stresses, in the analysis of arteries under physiological loading conditions substantially reduces the variation in circumferential and axial stresses [46, 50]. Since residual stresses significantly affect the overall stress state in the tissue, they also have a large impact on the *in vivo* state, the development, and the remodeling processes of arterial tissue.

Characterization of residual stresses was initially performed by the so-called 'opening angle' determined from a classical residual stress experiment (cf., e.g., [15]). For this purpose, an arterial segment is cut radially, resulting in the spring open and subsequent relaxation to an equilibrium configuration, which is assumed to be stress-free. Improvements in experiments clearly demonstrate, that residual deformations are three-dimensional and therefore cannot be described by a single two-dimensional parameter such as the 'opening angle' [26]. The authors in [26] harvested 16 pairs of rings (cut in radial direction) and axial strips of 11 abdominal aortas. After 16 h of relaxation images of the resulting geometry were taken and specimens were separated into the three individual layers; after another
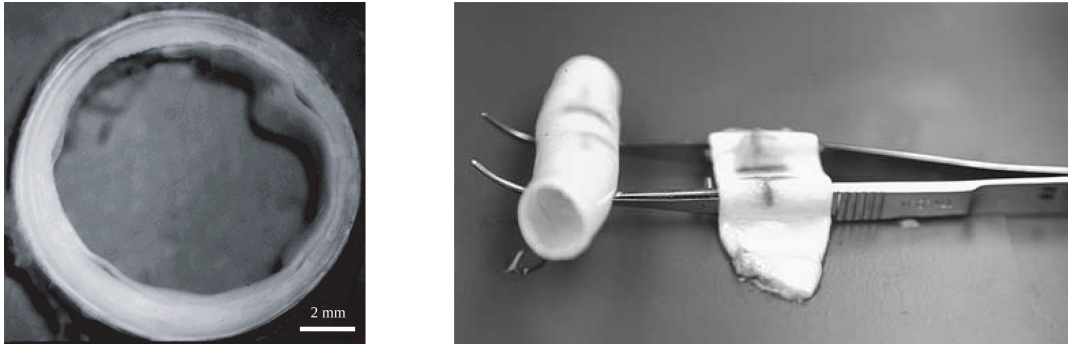
Figure 1.3: Spontaneous buckling of the intima in an iliac artery indicating the existence of compressive circumferential stress within the layer [26] (left panel). Separated intima-media tube-like structure suggesting the transition of compressive to tensile circumferential stresses and limp adventitia of an iliac artery [24] (right panel).

6 h images were recorded and analyzed, identifying axial and circumferential stretches and curvatures for every individual arterial layer. In [25] authors used axial and circumferential stretches and curvatures to perform the first analysis of the three-dimensional residual stress state in an aortic wall consisting of the three individual layers, modeled as circular cylindrical tubes and a rectangular cuboid. They provide analytic relations for stretches and stresses as a function of the radial position within every individual layer using the theory of nonlinear elasticity.

1.3 Continuum Mechanical Framework

Mechanical modeling of the extraordinary complex structure of soft biological tissues requires a framework, in which various physical phenomena can be described without detailed knowledge about the structure and/or microstructure. Therefore, the method of continuum mechanics, in which a certain material is treated as a macroscopic system, is used to approximate the individual constituents of soft biological tissue. This represents an average over certain dimensions, small enough to capture a particular behavior and reflect the material to the desired degree. Basic formulations are presented in the following for completeness of this thesis. The reader is referred to the book by Holzapfel [22] and references therein for a more detailed background on nonlinear continuum mechanics.

1.3.1 Kinematics

The continuum theory has developed independently of atomistic or molecular theory and assumes that a body $\mathcal{B}$ consists of certain matter at least piecewise continuously distributed in space and time. It is a composite of discrete particles P_k, where $\mathcal{B} = \{P_k\}$, embedded in the three-dimensional Euclidean space with fixed origin O and orthonormal basis vectors

$\mathbf{e}_i$, $i = 1, 2, 3$, as indicated in Fig. 1.4. At time t_0, the reference time, the continuum body $\mathcal{B}$ occupies the region Ω_0, which is referred to as the reference (or undeformed) configuration. A particular particle P within the prescribed region Ω_0 is defined by $\mathbf{X}(P, t_0)$. Over any time $t > t_0$ the continuum body $\mathcal{B}$ might have transformed into a new region denoted by Ω called current (or deformed) configuration. The position of the distinct particle P in the current configuration is given by $\mathbf{x} = \boldsymbol{\chi}(\mathbf{X}, t)$, where $\boldsymbol{\chi}$ is the motion of the continuum body $\mathcal{B}$. Thus, the deformation gradient can be defined as

$$\mathbf{F}(\mathbf{X}, t) = \frac{\partial \boldsymbol{\chi}(\mathbf{X}, t)}{\partial \mathbf{X}}, \tag{1.1}$$

a crucial quantity in nonlinear continuum mechanics characterizing the behavior of motion in the neighborhood of a particular point. Closer examination of (1.1) leads to the finding that the deformation gradient is a two-point tensor mapping points from the reference configuration to the current configuration. It serves as a linear transformation rule of a vector (line element) $d\mathbf{X}$ in the reference configuration to the vector (line element) $d\mathbf{x}$ in the current configuration, i.e.,

$$d\mathbf{x} = \mathbf{F}(\mathbf{X}, t) d\mathbf{X}. \tag{1.2}$$

The deformation gradient $\mathbf{F}$ is a nonsingular and invertible (i.e., $\det \mathbf{F} \neq 0$) second-order tensor. Its inverse $\mathbf{F}^{-1}$ represents the transformation of the vector $d\mathbf{x}$ in the current to the vector $d\mathbf{X}$ in the reference configuration. In general, the deformation gradient $\mathbf{F}$ depends on and varies with the reference coordinate $\mathbf{X}$, leading to a so-called inhomogeneous deformation. For the special case of a homogeneous deformation $\mathbf{F}$ is independent of any reference coordinate $\mathbf{X}$ and the associated motion is termed affine. The determinant of the deformation gradient $J(\mathbf{X}, t) = \det \mathbf{F} > 0$ is a measure of volume change due to applied deformation, i.e.,

$$dv = J dV, \tag{1.3}$$

where dv and dV represent infinitesimal volume elements in the current and the reference configuration, respectively. In the limit of an isochoric (volume preserving) deformation, the Jacobian determinant approaches $J = 1$ (e.g., during rigid-body motion). This quantity is also important in the well-known relationship called Nanson's formula, transforming surface area elements according to

$$d\mathbf{s} = J \mathbf{F}^{-\mathrm{T}} d\mathbf{S}, \tag{1.4}$$

where $d\mathbf{S} = \mathbf{N} dS$ and $d\mathbf{s} = \mathbf{n} ds$ denote the infinitesimal surface area elements, $\mathbf{N}$ and $\mathbf{n}$ the outward normals and dS and ds the area of the surface elements in the reference and current configuration, respectively.

The local motion defined by the deformation gradient $\mathbf{F}$ can be decomposed into pure stretch and pure rotation via the polar decomposition theorem. Thus,

$$\mathbf{F} = \mathbf{R}\mathbf{U} = \mathbf{v}\mathbf{R}, \tag{1.5}$$
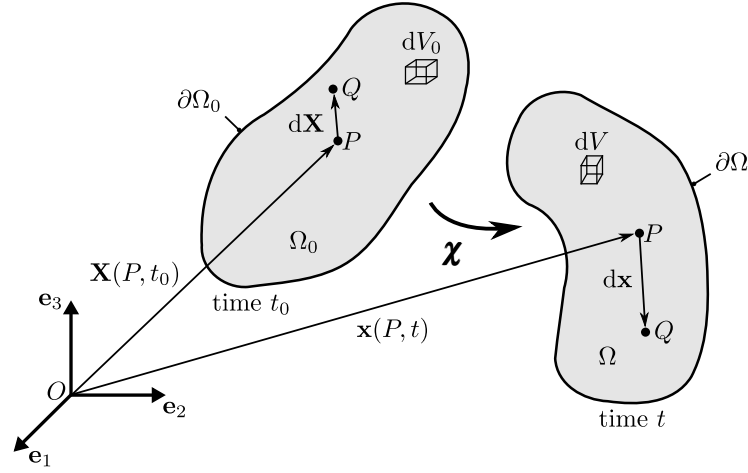
Figure 1.4: Schematic representation of reference Ω_0 and current Ω configuration indicating the associated motion $\boldsymbol{\chi}$. Taken with permission from [11].

where $\mathbf{U}$ and $\mathbf{v}$ are unique, positive definite, and symmetric tensors denoted as right and left stretch tensors, respectively. The second-order tensor $\mathbf{R}$ is a unique and proper orthogonal rotation tensor having the properties $\det\mathbf{R} = 1$ and $\mathbf{R}^{\mathrm{T}}\mathbf{R} = \mathbf{I}$, where $\mathbf{I}$ represents the second-order identity tensor. It is worth to mention that the right stretch tensor $\mathbf{U}$ is related to the reference, whereas the left stretch tensor $\mathbf{v}$ is connected to the current configuration. For completeness, relationship $(1.5)_1$ is referred as the right and relationship $(1.5)_2$ as the left polar decomposition.

Kinematic displacements are measurable quantities during the deformation of a body. In order to simplify analysis, the concept of strain is introduced. Therefore, the squares of the stretch tensors are given by

$$\mathbf{C} = \mathbf{F}^{\mathrm{T}}\mathbf{F} = \mathbf{U}^2 \qquad \text{and} \qquad \mathbf{b} = \mathbf{F}\mathbf{F}^{\mathrm{T}} = \mathbf{v}^2, \tag{1.6}$$

where $\mathbf{C}$ and $\mathbf{b}$ are denoted as the symmetric and positive definite right and left Cauchy-Green tensor, respectively. In both measures any resulting rigid body motion is eliminated, leading to the second-order identity tensor $\mathbf{I}$ for this specific type of motion.

1.3.2 Concept of Stress

In order to quantify the effect of deformation on a body, the concept of stress is introduced in the following. In contrast to force, which is a measurable physical quantity, stress is a mathematical concept to identify interactions between material points inside a continuum body $\mathcal{B}$ occupying the region Ω at time t with boundary surface $\partial\Omega$. It is claimed that there exists a surface traction, the so-called Cauchy traction vector $\mathbf{t}(\mathbf{x}, t, \mathbf{n})$, so that $\mathrm{d}\mathbf{f} = \mathbf{t}\mathrm{d}s$ holds, where $\mathrm{d}\mathbf{f}$ is an infinintesimal force vector and $\mathrm{d}s$ is a infinitesimal surface area

element in the current configuration. Deploying Cauchy's stress theorem with $\mathbf{n}$ being the unit outward normal in the current configuration given by

$$\mathbf{t} = \boldsymbol{\sigma}\mathbf{n} \tag{1.7}$$

leads to the definition of the symmetric Cauchy stress tensor $\boldsymbol{\sigma}$, i.e., $\boldsymbol{\sigma} = \boldsymbol{\sigma}^{\mathrm{T}}$. In continuum mechanics different stress tensors for various applications have been proposed. The most important ones used in computational mechanics are discussed in the following. The first Piola-Kirchhoff stress tensor can be computed by utilization of the Piola transformation (a passage between $\boldsymbol{\sigma}$ and $\mathbf{P}$), leading to

$$\mathbf{P} = J\boldsymbol{\sigma}\mathbf{F}^{-\mathrm{T}}, \tag{1.8}$$

where $\mathbf{P}$ is in general a nonsymmetric two-point tensor, similar to the deformation gradient $\mathbf{F}$, referred to the reference as well as the current configuration. Its transpose is frequently termed to as the nominal stress tensor. The Kirchhoff stress tensor $\boldsymbol{\tau} = J\boldsymbol{\sigma}$ is a stress measure often used in nonlinear FE analysis and related to the Cauchy stress tensor $\boldsymbol{\sigma}$ via the volume ratio J. Another important quantity in computational mechanics and especially useful for the formulation of constitutive equations is the second Piola-Kirchhoff tensor

$$\mathbf{S} = J\mathbf{F}^{-1}\boldsymbol{\sigma}\mathbf{F}^{-\mathrm{T}} = \mathbf{F}^{-1}\mathbf{P} = \mathbf{F}^{-1}\boldsymbol{\tau}\mathbf{F}^{-\mathrm{T}}, \tag{1.9}$$

a measure of stress associated with material coordinates having the property $\mathbf{S} = \mathbf{S}^{\mathrm{T}}$.

1.3.3 Classical Balance Principles

In the following, classical balance principles will be introduced for completeness of this thesis. Details on the derivation will be omitted and only essential relations are presented and discussed.

Reynold's Transport Theorem.   A fundamental theorem in classical continuum mechanics is Reynold's transport theorem. A spatial scalar field $\Phi = \Phi(\mathbf{x},t)$ is considered, which describes some physical quantity of a continuum body having the volume v at time t and occupying the region Ω with boundary $\partial\Omega$. If the considered spatial scalar field $\Phi(\mathbf{x},t)$ is continuously differentiable (i.e., it is smooth), the change of $\Phi(\mathbf{x},t)$ with respect to time t can be given via Reynold's transport theorem as

$$\frac{\mathrm{D}}{\mathrm{D}t}\int_{\Omega}\Phi(\mathbf{x},t)\mathrm{d}v = \int_{\partial\Omega}\Phi(\mathbf{x},t)\mathbf{v}(\mathbf{x},t)\cdot\mathbf{n}(\mathbf{x},t)\mathrm{d}s + \int_{\Omega}\frac{\partial\Phi(\mathbf{x},t)}{\partial t}\mathrm{d}v, \tag{1.10}$$

where the first term on the right-hand side of (1.10) represents the rate of outward normal flux $\Phi(\mathbf{x},t)\mathbf{v}$ across the surface $\partial\Omega$ and the second term corresponds to the change of $\Phi(\mathbf{x},t)$ within the considered region of interest Ω. The quantities $\mathbf{n}(\mathbf{x},t)$ and $\mathbf{v}(\mathbf{x},t)$ denote the outward unit normal field and the spatial velocity field, respectively.

Balance of Mass.   The fundamental physical property mass denoted by m is a measurable scalar quantity of a continuum body $\mathcal{B}$ distributed continuously over a certain region Ω with boundary surface $\partial\Omega$ at time t. The mass of a body can be determined by

$$m = \int_{\Omega} \rho(\mathbf{x},t)\mathrm{d}v, \tag{1.11}$$

where $\rho(\mathbf{x},t)$ is the spatial mass density and $\mathrm{d}v$ represents an infinitesimal volume element of the continuum body. In a closed system without any mass sources or mass sinks it is found that

$$\frac{\mathrm{D}m}{\mathrm{D}t} = \frac{\mathrm{D}}{\mathrm{D}t}\int_{\Omega} \rho(\mathbf{x},t)\mathrm{d}v = 0, \tag{1.12}$$

a fundamental statement in mechanics known as the conservation of mass. In various specific fields of mechanics it is necessary to discard the aforementioned assumption and investigate open systems, i.e., systems of a fixed amount of volume. In this case any mass can cross the boundary surface $\partial\Omega$, which can be expressed as

$$\frac{\mathrm{D}m}{\mathrm{D}t} = \frac{\mathrm{D}}{\mathrm{D}t}\int_{\Omega} \rho(\mathbf{x},t)\mathrm{d}v = \int_{\Omega} \frac{\partial\rho(\mathbf{x},t)}{\partial t}\mathrm{d}v. \tag{1.13}$$

Application of the divergence theorem and further rearrangement leads to the conservation of mass for a given control volume. Thus,

$$\frac{\mathrm{D}m}{\mathrm{D}t} = \frac{\mathrm{D}}{\mathrm{D}t}\int_{\Omega} \rho(\mathbf{x},t)\mathrm{d}v = -\int_{\partial\Omega} \rho(\mathbf{x},t)\mathbf{v}(\mathbf{x},t)\cdot\mathbf{n}\mathrm{d}s \tag{1.14}$$

is obtained. This equation concludes that the overall material time derivative is equal to the flux $\rho(\mathbf{x},t)\mathbf{v}(\mathbf{x},t)$ into the region Ω across its boundary surface $\partial\Omega$.

Balance of Linear and Angular Momentum.   Balance of linear and angular momentum are fundamental mechanical axioms, essential in continuum mechanics, valid for arbitrary regions Ω with boundary surface $\partial\Omega$ at time t as well as for the whole continuum body $\mathcal{B}$ under consideration. They are the direct consequence of Newton's second law of motion. In the following, $\mathbf{b}(\mathbf{x},t)$ denotes a spatial vector field called body force, which acts on the region Ω and represents, e.g., a gravity load or an electromagnetic load per unit volume. In addition, $\mathbf{t}(\mathbf{x},t,\mathbf{n})$ describes the already introduced Cauchy traction vector, a spatial vector field, acting on the surface boundary $\partial\Omega$ and let $\mathbf{v}(\mathbf{x},t)$ be a spatial velocity field. Thus, the relation

$$\frac{\mathrm{D}}{\mathrm{D}t}\int_{\Omega} \rho(\mathbf{x},t)\mathbf{v}(\mathbf{x},t)\mathrm{d}v = \int_{\partial\Omega} \mathbf{t}(\mathbf{x},t,\mathbf{n})\mathrm{d}s + \int_{\Omega} \mathbf{b}(\mathbf{x},t)\mathrm{d}v \tag{1.15}$$

is retrieved, which is denoted as the balance of linear momentum. Application of the divergence theorem leads to the global form of Cauchy's first equation of motion given as

$$\int_{\Omega} (\operatorname{div}\boldsymbol{\sigma}(\mathbf{x},t) + \mathbf{b}(\mathbf{x},t) - \rho(\mathbf{x},t)\dot{\mathbf{v}}(\mathbf{x},t))\mathrm{d}v = \mathbf{0}. \tag{1.16}$$

This relation holds for any current volume v and hence the local form under the assumption of zero acceleration, i.e., $\mathbf{a}(\mathbf{x},t) = \dot{\mathbf{v}}(\mathbf{x},t) = \mathbf{0}$, can be given by

$$\operatorname{div}\boldsymbol{\sigma}(\mathbf{x},t) + \mathbf{b}(\mathbf{x},t) = \mathbf{0}, \tag{1.17}$$

representing the Cauchy's equation of equilibrium in elastostatics. Introduction of the position vector $\mathbf{r}(\mathbf{x}) = \mathbf{x} - \mathbf{x}_0$ in conjunction with the aforementioned quantities leads to

$$\frac{\mathrm{D}}{\mathrm{D}t}\int_{\Omega} \mathbf{r}(\mathbf{x}) \times \rho(\mathbf{x},t)\mathbf{v}(\mathbf{x},t)\mathrm{d}v = \int_{\partial\Omega} \mathbf{r}(\mathbf{x}) \times \mathbf{t}(\mathbf{x},t,\mathbf{n})\mathrm{d}s + \int_{\Omega} \mathbf{r}(\mathbf{x}) \times \mathbf{b}(\mathbf{x},t)\mathrm{d}v, \tag{1.18}$$

known to be the balance of angular momentum in spatial description and serving as the starting point for the proof of symmetry of the Cauchy stress tensor, i.e., $\boldsymbol{\sigma} = \boldsymbol{\sigma}^{\mathrm{T}}$, omitted here.

Balance of Mechanical Energy. The last balance equation presented in this section concerns the balance of mechanical energy. Therefore, all other forms of energy, e.g., thermal, chemical, electrical, etc., are neglected in the following. Assuming a continuum body occupying the region Ω with boundary surface $\partial\Omega$, the balance of mechanical energy can be given by

$$\frac{\mathrm{D}}{\mathrm{D}t}\int_{\Omega} \frac{1}{2}\rho\mathbf{v}^2\mathrm{d}v + \int_{\Omega} \boldsymbol{\sigma}:\mathbf{d}\mathrm{d}v = \int_{\partial\Omega} \mathbf{t}\cdot\mathbf{v}\mathrm{d}s + \int_{\Omega} \mathbf{b}\cdot\mathbf{v}\mathrm{d}v. \tag{1.19}$$

In relation (1.19) the rate of change in kinetic energy, represented by the first term on the left-hand side, plus the work performed by internal stresses, represented by the second term on the left-hand side, is equal to any external work, i.e., any work performed by body force $\mathbf{b}(\mathbf{x},t)$ or surface traction $\mathbf{t}(\mathbf{x},t,\mathbf{n})$ acting on the considered continuum body. All quantities in (1.19) have been introduced and discussed earlier despite the so-called rate of deformation tensor $\mathbf{d}(\mathbf{x},t)$.

1.3.4 Constitutive Equations

Fundamental relations presented in previous paragraphs such as the kinematics, stresses, and balance principles are general equations, valid in any branch of continuum mechanics, e.g., fluid as well as solid mechanics. The main difference between these specific areas of continuum mechanics is the medium under consideration, which are liquids and gases (e.g., water, air, etc.) and solids (e.g., rubber, wood, etc.), respectively. Quantification of a certain stress state within a continuum medium through the presented kinematic relations

requires so-called constitutive equations, which approximate the behavior and the structure of the medium to a certain degree under specific conditions. In the following, fundamental relations for phenomenological constitutive equations are presented. These constitutive equations are mathematical models, which need to be fitted to experimental data in order to describe the material up to an acceptable degree. In particular, constitutive models in the regime of large, i.e., finite, strains are considered via nonlinear continuum mechanics. This results in so-called hyperelastic materials, claiming the existence of a Helmholtz free-energy function Ψ defined per unit reference volume. Further analysis assumes that the considered material is distributed in homogeneous manner within the continuum, i.e., the Helmholtz free-energy function Ψ does not depend on the material point as it is the case for heterogeneous materials. It is assumed that the scalar-valued Helmholtz free-energy function (also called strain-energy function (SEF)) depends on the deformation gradient $\mathbf{F}$, i.e., $\Psi = \Psi(\mathbf{F})$, where the relation

$$\mathbf{P} = \frac{\partial \Psi(\mathbf{F})}{\partial \mathbf{F}} \tag{1.20}$$

is postulated. This relation for the first Piola-Kirchhoff stress $\mathbf{P}$ can be rewritten in terms of the Cauchy stress tensor $\boldsymbol{\sigma}$ using the Piola transformation as

$$\boldsymbol{\sigma} = J^{-1} \frac{\partial \Psi(\mathbf{F})}{\partial \mathbf{F}} \mathbf{F}^{\mathrm{T}}. \tag{1.21}$$

In order to ensure fundamental consistency in continuum mechanics, constitutive material models need to fulfill several restrictions. In the absence of any deformation, e.g., where $\mathbf{F} = \mathbf{I}$, the strain-energy must vanish according to $\Psi = \Psi(\mathbf{I}) = 0$. Furthermore, physical observations lead to the finding that the strain-energy increases with deformation, which requires $\Psi = \Psi(\mathbf{F}) \geq 0$. Another restriction on Ψ is objectivity, meaning that the strain-energy does not change under rigid body motion, i.e., neither translation nor rotation. This requires the SEF to hold for

$$\Psi(\mathbf{F}) = \Psi(\mathbf{U}) = \Psi(\mathbf{C}). \tag{1.22}$$

An isotropic hyperelastic material may also be described in terms of the independent strain invariants of the symmetric right Cauchy-Green tensor $\mathbf{C}$, where its eigenvalues are the squares of the principal stretches λ_i^2, $i = 1,2,3$. Hence, the SEF can be expressed as

$$\Psi = \Psi[I_1(\mathbf{C}), I_2(\mathbf{C}), I_3(\mathbf{C})], \tag{1.23}$$

where the invariants are given by

$$I_1(\mathbf{C}) = \mathrm{tr}\mathbf{C} = \lambda_1^2 + \lambda_2^2 + \lambda_3^2, \tag{1.24}$$

$$I_2(\mathbf{C}) = \frac{1}{2}[(\mathrm{tr}\mathbf{C})^2 - \mathrm{tr}(\mathbf{C}^2)] = \lambda_1^2\lambda_2^2 + \lambda_1^2\lambda_3^2 + \lambda_2^2\lambda_3^2, \tag{1.25}$$

$$I_3(\mathbf{C}) = \det\mathbf{C} = \lambda_1^2\lambda_2^2\lambda_3^2. \tag{1.26}$$

In the case of an anisotropic material, a material exhibiting directional dependency, e.g., two preferred directions denoted by $\mathbf{a}_0$ and $\mathbf{g}_0$ in the reference and $\mathbf{a}$ and $\mathbf{g}$ in the current configuration, the so-called pseudo-invariants $I_4, \ldots, I_9$ might be used to fully describe the material. The invariant I_9 is not considered since it represents a geometrical constant and does not depend on the deformation. Furthermore, experimental insight is limited, leading to usage of the convenient pseudo-invariants I_4 and I_6, which can be introduced to be

$$I_4(\mathbf{C}, \mathbf{a}_0) = \mathbf{a}_0 \cdot \mathbf{C}\mathbf{a}_0 = \mathbf{C} : \mathbf{A}_0 = \lambda_{\mathrm{a}}^2, \tag{1.27}$$

$$I_6(\mathbf{C}, \mathbf{g}_0) = \mathbf{g}_0 \cdot \mathbf{C}\mathbf{g}_0 = \mathbf{C} : \mathbf{G}_0 = \lambda_{\mathrm{g}}^2, \tag{1.28}$$

where λ_{a} and λ_{g} are the stretches in the preferential directions and $\mathbf{A}_0 = \mathbf{a}_0 \otimes \mathbf{a}_0$ and $\mathbf{G}_0 = \mathbf{g}_0 \otimes \mathbf{g}_0$ are the structural tensors. By means of these two additional invariants a SEF does not only depend on the deformation gradient $\mathbf{F}$, but also on the preferred directions defined in the reference configuration via unit vectors $\mathbf{a}_0(\mathbf{X})$ and $\mathbf{g}_0(\mathbf{X})$. Thus, the SEF can be postulated as

$$\Psi = \Psi(\mathbf{C}, \mathbf{A}_0, \mathbf{G}_0). \tag{1.29}$$

Differentiation of the proposed SEF with respect to the right Cauchy-Green $\mathbf{C}$ will provide an equation for the second Piola-Kirchoff stress tensor $\mathbf{S}$. Application of the chain rule of differentiation leads to

$$\mathbf{S} = 2\frac{\partial \Psi(\mathbf{C}, \mathbf{A}_0, \mathbf{G}_0)}{\partial \mathbf{C}} = 2\sum_{i=1}^{8} \frac{\partial \Psi(I_1, I_2, \ldots, I_8)}{\partial I_i} \frac{\partial I_i}{\partial \mathbf{C}}. \tag{1.30}$$

1.3.5 Modeling of Incompressibility

Various different materials (e.g., water, polymers, biological tissue, etc.) can sustain finite deformation without any noticeable change in volume. Such materials are denoted to be incompressible and the associated motion is referred to be isochoric. Modeling incompressibility in FE analysis is often performed by the application of a compressible formulation, where the (near) incompressibility is enforced by a penalization of a volumetric term. Therefore, the deformation gradient $\mathbf{F}$ is multiplicatively decomposed into a volume-changing (volumetric) $J^{1/3}\mathbf{I}$ and a volume-preserving (isochoric) $\overline{\mathbf{F}}$ part given by

$$\mathbf{F} = (J^{1/3}\mathbf{I})\overline{\mathbf{F}} = J^{1/3}\overline{\mathbf{F}}, \tag{1.31}$$

where $\overline{\mathbf{F}}$ is denoted as the modified deformation gradient. Similarly, the isochoric or modified right and left Cauchy-Green tensor may be retrieved by

$$\mathbf{C} = (J^{2/3}\mathbf{I})\overline{\mathbf{C}} = J^{2/3}\overline{\mathbf{C}} \quad \text{and} \quad \mathbf{b} = (J^{2/3}\mathbf{I})\overline{\mathbf{b}} = J^{2/3}\overline{\mathbf{b}}, \tag{1.32}$$

respectively. Thus, the decoupled representation of the SEF is specified as

$$\Psi(\mathbf{C}) = \Psi_{\mathrm{vol}}(J) + \Psi_{\mathrm{iso}}(\overline{\mathbf{C}}), \tag{1.33}$$

where $\Psi_{\text{vol}}(J)$ and $\Psi_{\text{iso}}(\overline{\mathbf{C}})$ describe the volumetric elastic and the isochoric elastic response, respectively.

Furthermore, application of the standard Coleman-Noll procedure leads to an additive spit of the stress response. In particular, the second Piola-Kirchhoff stress $\mathbf{S}$ can be additively decomposed to

$$\mathbf{S} = 2\frac{\partial \Psi(\mathbf{C})}{\partial \mathbf{C}} = \mathbf{S}_{\text{vol}} + \mathbf{S}_{\text{iso}}, \tag{1.34}$$

where the terms $\mathbf{S}_{\text{vol}}$ and $\mathbf{S}_{\text{iso}}$ denote the purely volumetric and the purely isochoric stress contribution. In addition, the individual terms are given by

$$\mathbf{S}_{\text{vol}} = 2\frac{\partial \Psi_{\text{vol}}(J)}{\partial \mathbf{C}} = Jp\mathbf{C}^{-1} \qquad \text{and} \qquad \mathbf{S}_{\text{iso}} = 2\frac{\partial \Psi_{\text{iso}}(\overline{\mathbf{C}})}{\partial \mathbf{C}} = J^{-2/3}\text{Dev}\overline{\mathbf{S}}, \tag{1.35}$$

where the fictitious second Piola-Kirchhoff stress $\overline{\mathbf{S}}$ and the hydrostatic pressure p are defined by

$$p = \frac{\text{d}\Psi_{\text{vol}}(J)}{\text{d}J} \qquad \text{and} \qquad \overline{\mathbf{S}} = 2\frac{\partial \Psi_{\text{iso}}(\overline{\mathbf{C}})}{\partial \overline{\mathbf{C}}}. \tag{1.36}$$

The deviatoric operator is defined as $\text{Dev}(\bullet) = (\bullet) - 1/3[(\bullet):\mathbf{C}]\mathbf{C}^{-1}$ in material coordinates so that

$$\text{Dev}\overline{\mathbf{S}} : \mathbf{C} = 0. \tag{1.37}$$

In the previous section the constitutive equation has been defined in terms of the independent strain invariants of the symmetric right Cauchy-Green tensor (I_1, I_2, and I_3) as well as the so-called pseudo-invariants ($I_4, \ldots, I_9$). Following the concept of isochoric and volumetric splitting, also these invariants need to be modified according to $(1.32)_1$. Thus, the subsequently important modified invariants $\bar{I}_1 = \text{tr}\overline{\mathbf{C}} = J^{-2/3}I_1$, $\bar{I}_4 = \overline{\mathbf{C}} : \mathbf{A}_0 = J^{-2/3}I_4$ and $\bar{I}_6 = \overline{\mathbf{C}} : \mathbf{G}_0 = J^{-2/3}I_6$ are obtained.

1.3.6 Elasticity Tensor

Computational implementation of nonlinear problems in finite elasticity requires incremental or iterative solution methods in connection with an adequate convergence criterion to obtain results with reasonable accuracy. These results are obtained by solving a sequence of linearized problems using the elasticity tensor $\mathbb{C}$, which may be defined in terms of the second Piola-Kirchhoff stress tensor $\mathbf{S}$ or the SEF of a particular material $\Psi(\mathbf{C})$. Thus,

$$\mathbb{C} = 2\frac{\partial \mathbf{S}(\mathbf{C})}{\partial \mathbf{C}} = 4\frac{\partial^2 \Psi(\mathbf{C})}{\partial \mathbf{C}\partial \mathbf{C}} \tag{1.38}$$

represents a relation for the elasticity tensor in material description. It characterizes the change in stress as a result of a change in strain and relates work conjugate pairs of stress and strain tensors. The elasticity tensor $\mathbb{C}$ possesses minor (holds for all elastic materials) and major (necessary and sufficient for hyperelasticity) symmetries. To continue the concept of (near) incompressibility, the decoupled representation of the elasticity tensor $\mathbb{C}$ in

a purely volumetric contribution $\mathbb{C}_{\mathrm{vol}}$ and a purely isochoric contribution $\mathbb{C}_{\mathrm{iso}}$ is given by $\mathbb{C} = \mathbb{C}_{\mathrm{vol}} + \mathbb{C}_{\mathrm{iso}}$. Individual components are found to be

$$\mathbb{C}_{\mathrm{vol}} = 2\frac{\partial \mathbf{S}_{\mathrm{vol}}}{\partial \mathbf{C}} \qquad \text{and} \qquad \mathbb{C}_{\mathrm{iso}} = 2\frac{\partial \mathbf{S}_{\mathrm{iso}}}{\partial \mathbf{C}}. \tag{1.39}$$

Consistent linearization is a prerequisite to preserve quadratic convergence of the solution and crucial in computational mechanics.

1.4 Finite Element Implementation

In the context of biomechanics and mechanobiology investigations of the impact of mechanical boundary conditions on the formation and the evolution of various diseases of biological tissues, e.g., such as AAA, are performed. The complex geometry as well as the nonlinear material behavior requires application of sophisticated numerical algorithms such as the FE method, in this thesis used to study stress states within a AAA wall and the ILT. Hence, general FE equations are provided in the following (residual stresses are neglected) including the strong and the weak form [11]. The static equilibrium mixed boundary-value problem in reference coordinates on the domain Ω_0 is given by

$$\mathrm{Div}(\mathbf{FS}) = \mathbf{0} \qquad \text{in} \qquad \Omega_0, \tag{1.40}$$

where $\mathrm{Div}(\bullet)$ defines the divergence operator with respect to the reference configuration. Systolic (maximum) and diastolic (minimum) pressure p acting on the AAA lumen surface $\partial\Omega_{0\mathbf{t}1}$ introduces traction boundary conditions to the boundary-value problem (traction due to blood flow is neglected), whereas the outer AAA wall $\partial\Omega_{0\mathbf{t}2}$ is assumed to be completely traction free (any connective tissue is assumed to have no influence on the AAA). In addition to that, numerous zero-displacement boundary conditions at different surfaces $\partial\Omega_{0\mathbf{u}1}$ and in different coordinate directions are applied to mimic the *in vivo* situation. This includes restrictions in vertical displacement at the transition zones of the AAA geometry to the connected parts of the abdominal aorta (top) and the common iliac arteries (bottom) as well as restrictions in circumferential movement at the intersection of the lumen surface with these transition zones. Thus,

$$\mathbf{FSN} = -pJ(\mathbf{F}^{-1})^{\mathrm{T}}\mathbf{N} \qquad \text{on} \qquad \partial\Omega_{0\mathbf{t}1}, \tag{1.41}$$

$$\mathbf{FSN} = \mathbf{0} \qquad \text{on} \qquad \partial\Omega_{0\mathbf{t}2}, \tag{1.42}$$

$$\mathbf{u}(\mathbf{X}) = \mathbf{0} \qquad \text{on} \qquad \partial\Omega_{0\mathbf{u}1}, \tag{1.43}$$

in which $\mathbf{N}$ defines the unit surface normal. It is important to emphasize that the pressure p denotes a so-called follower load, i.e., a deformation dependent load. Hence, the principal of virtual work might, in general, not be used as the basic framework for the FE method.

Without any further derivation, the weak equilibrium formulation

$$\int_{\Omega_0} \text{Tr}[\mathbf{S}(\mathbf{F}^\text{T}\text{Grad}\boldsymbol{\phi})^\text{S}]\text{d}v + \int_{\partial\Omega_{0t1}} pJ(\mathbf{F}^{-1})^T\mathbf{N}\cdot\boldsymbol{\phi}\text{d}A = 0 \qquad \text{in} \qquad \Omega_0 \qquad (1.44)$$

$$\mathbf{u}(\mathbf{X}) = \mathbf{0} \qquad\qquad\qquad\qquad \text{on} \qquad \partial\Omega_{0\mathbf{u}1} \qquad (1.45)$$

needs to be fulfilled, where $\text{Tr}(\bullet)$ and $\text{Grad}(\bullet)$ represent the trace and the gradient operator in reference coordinates, respectively. Furthermore, $\boldsymbol{\phi}$ is a suitable vector-valued test function satisfying prescribed displacement boundary conditions. The multipurpose FE software package FEAP (University of California, Berkeley, CA) with an implemented iterative Newton-Raphson solver is used to calculate the unknown displacements $\mathbf{u}$ associated with the given pressure p. Isoparametric hexahedral elements based on a three-field Hu-Washizu variational formulation (mixed Q1/P0-elements) provide a proper framework to model tissue components.

2 MATERIALS AND METHODS

2.1 Magnetic Resonance Imaging

Recent progress in medical imaging improved the support of clinicians in diagnosis and subsequent treatment of various diseases in different stages. New technologies and methods in MRI, as well as CTA, enhance soft tissue contrast and enable to distinguish between the structures of interest. In particular, different acquisition protocols in MRI opened up the possibility to differentiate between the AAA wall and the ILT within the context of AAA imaging (see Fig. 2.1(b)) and hence this was the imaging method of choice. Other advantages of MRI over CTA include, e.g., the lack of ionizing radiation and nephrotoxic contrast agents and increased sensitivity to endoleaks [20].

Patients suffering from a AAA with a diameter larger than 5 cm were selected from the outpatient clinic of the University Hospital of Leuven. If no contraindications were detected, MRI studies have been performed using a 1.5 T scanner (Aera; Siemens, Erlangen, Germany) on every patient. Therefore, a sagittal and a transversal balanced steady-state free precession (bSSFP) sequence served as localizers using 20/30 slices, 5/6 mm slice thickness, no intersection gap, a field of view (FOV) of 380 mm, a matrix size of 320×260, the quantities time to repetition/time to echo (TR/TE) of 4.41 ms/2.21 ms and one signal average. In addition, a pulse triggered, three slice T1 Turbo Spin Echo (TSE) sequence with a thickness of 6 mm, TR/TE = 800/62 ms, FOV of 160 mm and a matrix size of 256×256 was conducted. Subsequent to intravenous administration of a standardized dose of 0.1 mmol/kg Gd-DOTA (Dotarem, Guerbet, France), a coronal breath-hold fast low-angle shot (FLASH) 3D sequence of 96 slices in the arterial phase with a slab thickness of 1.25 mm, 384×336 matrix size, TR/TE = 3.04/1.09 ms and a FOV of 400 mm was performed. The MRI study was registered at the clinical trial center of the University Hospitals of Leuven (study number S52774) and ethical approval was obtained from the ethical committee UZ Leuven.

Visual evaluation of image quality and tissue contrast between the AAA wall and the ILT was performed with clinicians to decide on the images taken for reconstruction. It transpired that the transversal bSSFP sequence (see Fig. 2.1) provided best results according to the demands for image analysis. Hence, this particular image sequence was chosen to perform image segmentation and reconstruction of the patient-specific AAA geometry.
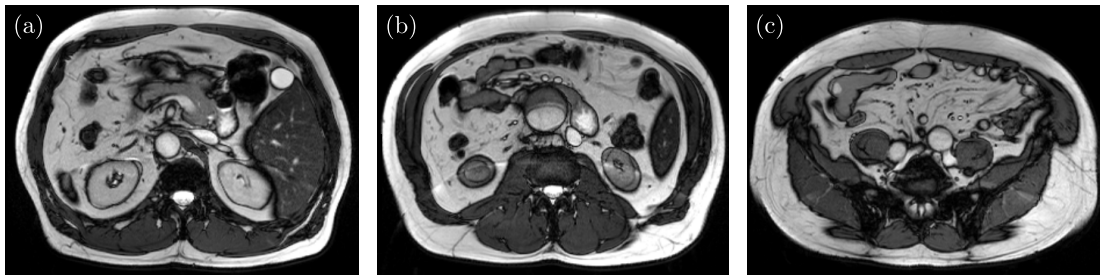
Figure 2.1: MRI slices obtained by application of the new acquisition protocol at different vertical positions of (a) the abdominal aorta without an ILT, (b) the AAA wall with corresponding ILT, and (c) the common iliac arteries.

2.2 Finite Element Mesh Generation

The generation of high-quality conforming meshes of the AAA wall and the ILT is of crucial importance in FE simulations. Various open source as well as commercial software packages are available to generate meshes of complex structures using tetrahedral elements for both computational fluid dynamics (CFD) and FE analysis applications, while automated structured hexahedral mesh generation is limited to simple geometries [9]. In general, the performance of hexahedral elements in FE simulations is superior to tetrahedrons or wedge elements, which may lead to severe locking problems and therefore appear too stiff [48]. This fact could cause serious impact on stress and displacement predictions and subsequent conclusions. Specific details on the mesh generation procedure, mainly performed by collaborators at the Departamento de Tecnología Fotónica y Bioingeniería at Universidad Politécnica de Madrid, are presented in [62].

2.2.1 Image Segmentation and Reconstruction

In order to obtain an accurate representation of the *in vivo* imaged AAA, transversal MRI slices are segmented manually to identify the contours of interest and generate patient-specific geometries. The manual segmentation is performed using the open source software application ITK-SNAP [72], where also semi-automatic segmentation using active contour methods and image navigation is provided. In the MRI images the outer arterial wall contour, the lumen contour, as well as the inner arterial wall contour where an ILT is present (all of them can be clearly recognized in Fig. 2.1(b)) are delineated, resulting in three binary images for every MRI slice (lumen contour and inner arterial wall contour coincide if no ILT is present). In addition to that, careful smoothing is performed on the contours of interest to eliminate possible inaccuracies in manual segmentation and preserve important structural information. The three binary images of every transversal MRI slice are placed at the vertical position of the slice being taken to reconstruct the patient-specific AAA wall and the ILT geometry.

2.2.2 Finite Element Meshing Protocol

In the literature, the standard procedure for meshing bifurcations is to divide them into independent vessel sections and generate meshes for each of them individually. In particular, the method proposed in [39] is modified, where similar approaches have been published in [4, 5]. Following this idea, a semi-automatic patient-specific algorithm is developed within the commercial software package MATLAB (Mathworks Inc., Natick, MA), generating conforming hexahedral meshes of the AAA wall and the ILT. Therefore, the volume of the AAA with the corresponding part of the ILT is subdivided into three individual vessels using three planes defined by five manually chosen points:

- Anterior Point: anterior cranial to the bifurcation on the lumen surface,
- Posterior Point: posterior cranial to the bifurcation on the lumen surface,
- Caudal Point: centered and caudal to the bifurcation on the wall surface,
- Dexter Point: dexter cranial to the bifurcation on the lumen surface,
- Sinister Point: sinister cranial to the bifurcation on the lumen surface.

The three-dimensional location of every individual point is crucial for the process of mesh generation since this dramatically affects element shape and hence also the mesh quality, which has a direct impact on FE simulation results as discussed earlier. Subsequent division of the three vessels into six sections (the vessel of the abdominal aorta is divided into a left and a right section, whereas both common iliac arteries are divided into an interior and an exterior section) is needed, where specific attention is required in order to achieve adequate meshes at the transition zones between independent sections.

The procedure of mesh generation is continued by the definition of three quadrilateral meshes, subsequently used to construct the FE mesh with conforming hexahedral elements. The first quadrilateral mesh is defined by the outer contour of the AAA wall (Fig. 2.2(c)), the second one is defined by the contour of the lumen (Fig. 2.2(a)), and for the third one the inner contour of the AAA wall is taken (Fig. 2.2(b)). Following these definitions and application of the developed semi-automatic algorithm, in which several parameters can be adjusted to tune mesh density, leads to the needed nodes defining the quadrilateral elements for these surface meshes. The final step includes the calculation of a center line using the lumen surface and the definition of a reference mesh (in this case the quadrilateral mesh of the outer contour of the AAA wall). This mesh is arbitrarily chosen and used as a reference to update the position of the nodes over the remaining meshes. Thus, for every node in the reference mesh a vector to its corresponding point at the center line is defined, intersecting with the mesh of the inner contour of the AAA wall at a particular position. At this intersection point a node for the updated mesh of the inner AAA wall surface is defined, leading to corresponding quadrilaterals at the outer and the inner boundaries of the AAA wall. These quadrilateral elements are joined to form the intended hexahedral elements. The ILT mesh is established by definition of another vector from every node of the updated mesh of the inner AAA wall surface to its corresponding point at
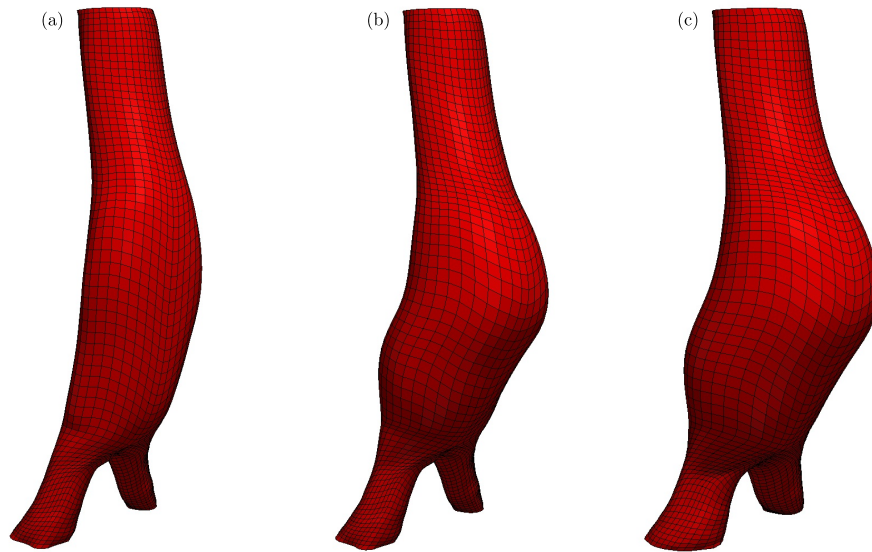
Figure 2.2: Quadrilateral element meshes of (a) the lumen surface, (b) the internal surface of the AAA wall, and (c) the outer surface of the AAA wall used for construction of conforming hexahedral FE meshes.

the center line. Again, at the intersection of every distinct vector with the lumen surface mesh a partner point is generated, leading to quadrilaterals, which are subsequently joined to form the hexahedral ILT mesh. In cases of the ILT not being present this method creates hexahedral elements with zero volume and no physical interpretation. These elements are removed in order to obtain the final conforming hexahedral FE mesh. Application of the proposed meshing algorithm generates elements with collapsed nodes, i.e., degenerated hexahedral elements (wedges, pyramids, etc.), located at the edge of the ILT. This is a necessity since the ILT is not present throughout the whole AAA. However, this concept has been extensively used in the past in FE analysis [73].

The aortic wall (cf., [17]) as well as the ILT (cf., [63]) constitute three distinct layers having different structures and different mechanical properties. To model these features, the two-layer hexahedral mesh generated for the AAA wall and the ILT, which is an accurate representation of the overall structure, is used. Every hexahedron for the AAA wall and the ILT is divided radially into three using empirically-determined thickness ratios, which represent the variability of the aortic wall and the ILT within the aneurysm. The ratios for the aortic wall are found to be 0.19 for the intima, 0.44 for the media, and 0.37 for the adventitia, and are in the range of values reported in [58]. Thickness ratios in the ILT are given by 0.24 for the luminal, 0.38 for the medial, and 0.38 for the abluminal layer,

representing possible measurements as they may have been determined in [63]. The developed semi-automatic FE meshing algorithm is capable to create meshes of any density and size. For instance, meshes with higher element density can be generated without significant increase in computation time. Once the five manually chosen points have been selected, generating a 25000 element mesh takes around 30 s using a 3 GHz Pentium Core Duo with 8 GB RAM. It is important to emphasize that the algorithm is robust in generating high quality hexahedral elements tested and validated for several patient-specific AAA geometries. However, speed optimization has not been performed.

2.2.3 Finite Element Mesh Quality Evaluation

In the process of FE mesh generation it is crucial to represent the original *in vivo* geometry with sufficient accuracy as well as to generate finite elements with satisfying element quality. This affects solution of partial differential equations (PDE)s and thus can have a large impact upon the accuracy as well as the efficiency of simulations [38]. The quality of a mesh includes several issues one has to consider when applying it to engineering methods such as the FE method. In particular, it depends on the type of calculation performed and might change when evaluating different calculations. A large variety of different finite element quality measurements for two- and three-dimensional structures have been presented throughout the last years for applications in CFD and FE analysis, e.g., see [13, 35–37]. Among all the metrics available as a measure of initial mesh quality, the scaled Jacobian is the most common one used in FE simulations for solid structures [9]. The open source program ParaView [21], a multi-platform data analysis and visualization application, is used to calculate and visualize scaled Jacobian values for FE mesh elements. This scientific software package uses the 'Verdict library' to evaluate different quality measurements, where mathematical specifications are given in [61]. Therefore, the 'Jacobian', the determinant of the discrete Jacobian matrix J_k, evaluated at the hexahedron's vertices $k = 1, 2, \ldots, 8$ and the center of the element $k = 0$, is the triple scalar product (also called mixed or box product) of the edges connected to that node ($\mathbf{e}_{k1}$, $\mathbf{e}_{k2}$, $\mathbf{e}_{k3}$) and of the principal axes of the element ($\mathbf{e}_{01}$, $\mathbf{e}_{02}$, $\mathbf{e}_{03}$), respectively, given by

$$J_k = \mathbf{e}_{k1}(\mathbf{e}_{k2} \times \mathbf{e}_{k3}). \tag{2.1}$$

The minimum after normalization of the Jacobian (division of the Jacobian by the length of the three corresponding vectors of an element) leads to the scaled Jacobian value

$$\text{Scaled Jacobian} = \min\left[\frac{J_k}{\|\mathbf{e}_{k1}\| \|\mathbf{e}_{k2}\| \|\mathbf{e}_{k3}\|}\right], \tag{2.2}$$

where the full range of a hexahedron's scaled Jacobian value is between -1 (worst) and $+1$ (best). Nevertheless, a positive value is the minimal quality permitted for analysis [9]. Negative scaled Jacobian values indicate the existence of inverted (invalid) elements in the FE mesh. An acceptable range for scaled Jacobian values is stated to be between 0.5 and

1 [61]. The scaled Jacobian mesh quality metric can only be applied to regular hexahedral elements having eight vertices at different spatial locations in three-dimensional space. Therefore, collapsed hexahedral elements are identified and excluded from the mesh quality analysis.

2.3 Constitutive Models

One of the fundamental issues in computational FE analysis of soft biological tissues is to model the response of the material, i.e., the AAA wall as well as the ILT, with the desired degree of accuracy. The representation of the material is crucial since simulation results should estimate *in vivo* stresses used for further conclusions on the impact of various physiological and pathophysiological conditions [54]. Nonlinear finite-strain constitutive models based on convex SEF are used to represent experimentally-determined responses of the different tissues considered. The SEF is split (see (1.33)) into an isochoric and a volumetric contribution, where the latter one is particularized as

$$\Psi_{\mathrm{vol}}(J) = \frac{\mu_{\mathrm{K}}}{2}(J-1)^2. \tag{2.3}$$

The variable μ_{K} represents a stress-like parameter, which degenerates to a non-physical, positive penalty parameter in the case of isochoric deformation to enforce incompressibility. Increasing μ_{K} reduces the violation of the incompressibility constraint, where in the limit of $\mu_{\mathrm{K}} \to \infty$ the constraint is exactly enforced and Ψ represents a functional for an incompressible material with $J = 1$. Thus, the penalty parameter is chosen to be $\mu_{\mathrm{K}} = \mu \cdot 10^3$ for FE simulations. The isochoric part of the SEF is further divided into an isotropic and an anisotropic contribution as

$$\Psi_{\mathrm{iso}}(\bar{I}_1, \bar{I}_4, \bar{I}_6) = \Psi_{\mathrm{m}}^k(\bar{I}_1) + \Psi_{\mathrm{f}}^k(\bar{I}_1, \bar{I}_4, \bar{I}_6), \tag{2.4}$$

where $k \in [\mathrm{a}, \mathrm{t}]$, for the AAA wall and the ILT, respectively. Explicit constitutive models representing the mechanical behavior of the AAA wall and the ILT are provided and discussed in the following.

Constitutive Model of the Aortic Wall.   The non-collagenous isotropic matrix material of the AAA wall, i.e., the aortic wall, is represented by use of the standard neo-Hookean material model given as

$$\Psi_{\mathrm{m}}^{\mathrm{a}}(\bar{I}_1) = \frac{\mu}{2}(\bar{I}_1 - 3), \tag{2.5}$$

where $\mu > 0$ is a stress-like material parameter known as the shear modulus in the reference configuration. The anisotropic and highly nonlinear response of the AAA wall due to the collagen fiber network is captured by [17]

$$\Psi_{\mathrm{f}}^{\mathrm{a}}(\bar{I}_1, \bar{I}_4, \bar{I}_6) = \frac{k_1}{2k_2} \sum_{i=4,6} \left\{ \exp\{k_2[\kappa\bar{I}_1 + (1-3\kappa)\bar{I}_i - 1]^2\} - 1 \right\}, \tag{2.6}$$

	μ [kPa]	k_1 [kPa]	k_2 [-]	ϕ [°]	κ [-]
intima	44.0	$10.14 \cdot 10^3$	0.00	40.5	0.25
media	28.0	$0.81 \cdot 10^3$	12.42	39.1	0.18
adventitia	10.0	$0.38 \cdot 10^3$	3.35	40.59	0.11

Table 2.1: Median material and structural parameters for the intima, the media, and the adventitia of the human abdominal aortic wall determined from 9 donors (mean age 61.0 ± 11 yr) [69]. Damage parameters r_f and m_f are neglected since they do not influence the primary loading curve.

where $k_1 > 0$ is a stress-like material parameter, $k_2 > 0$ is a dimensionless parameter controlling the degree of non-linearity of the fiber fabric response, and $\kappa \in [0, 1/3]$ is a dimensionless parameter representing the rotationally symmetric dispersion of the collagen fiber orientations around the principal directions $\mathbf{a}_0$ and $\mathbf{g}_0$ in the reference configuration, with $\|\mathbf{a}_0\| = \|\mathbf{g}_0\| = 1$. In this particular constitutive equation the term

$$\bar{I}_i^\star = \kappa \bar{I}_1 + (1 - 3\kappa)\bar{I}_i, \qquad i = 4, 6, \tag{2.7}$$

is used to distinguish between tension and compression of collagen fibers [68]. Therefore, (2.6) only contributes to the SEF of the aortic wall if $\bar{I}_4^\star > 1$ or $\bar{I}_6^\star > 1$. In the limit of the dispersion parameter $\kappa = 0$, the proposed material model degenerates to the constitutive equation presented in [24], modeling a structure with perfectly aligned fibers, whereas in the other limiting case, i.e., $\kappa = 1/3$, the expression corresponds to an isotropic distribution similar to that of [10].

The principal directions of anisotropy, i.e., the collagen fiber directions $\mathbf{a}_0$ and $\mathbf{g}_0$, in the reference configuration are symmetrically oriented with respect to the circumferential direction of the aortic wall. Thus, both directions are uniquely defined by the structural parameter ϕ, a parameter defining the in plane fiber angle with respect to the local circumferential direction. Table 2.1 provides model parameters μ, k_1, k_2, ϕ and κ for the intima, the media, and the adventitia of the AAA wall determined from 9 donors (mean age 61.0 ± 11 yr) [69].

Constitutive Model of the Intraluminal Thrombus. Similar to the constitutive material model for the AAA wall, the isotropic material composite of the ILT is represented by a neo-Hookean model given as

$$\Psi_m^t(\bar{I}_1) = \mu(\bar{I}_1 - 3), \tag{2.8}$$

where $\mu > 0$ is again a stress-like material parameter known as twice the shear modulus of the underlying material in the reference configuration. Observations in [63] suggest that the individual ILT layers, i.e., the luminal, the medial, and the abluminal layer, exhibit distinct

	μ [kPa]	k_1 [kPa]	k_2 [-]	ϕ [°]	ρ [-]
luminal	9.7	15.9	2.7	84.1	0.33
medial	7.1	6.0	0.07	86.7	0.05
abluminal	5.1	2.9	0.03	89.1	0.05

Table 2.2: Mean material and structural parameters for the luminal (anisotropic), the medial, and the abluminal layers of human ILT determined from 43 AAA samples (mean age 67.0 ± 6 yr) [63].

nonlinear mechanical properties. Remarkable anisotropy can only be found in some of the luminal layers. Thus, the tissue response is captured phenomenologically by [27]

$$\Psi_{\mathrm{f}}^{\mathrm{t}}(\bar{I}_1, \bar{I}_4, \bar{I}_6) = \frac{k_1}{2k_2} \sum_{i=4,6} \left\{ \exp\{k_2[(1-\rho)(\bar{I}_1 - 3)^2 + \rho(\bar{I}_i - 1)^2]\} - 1 \right\}, \qquad (2.9)$$

where again $k_1 > 0$ is a stress-like material parameter, $k_2 > 0$ is a dimensionless parameter controlling the degree of non-linearity, and $\rho \in [0,1]$ is a dimensionless weighting factor between isotropic and anisotropic response. The constitutive model in (2.9) needs specification of preferred directions within the ILT defined by the vectors $\mathbf{a}_0$ and $\mathbf{g}_0$ in the reference configuration, with $\|\mathbf{a}_0\| = \|\mathbf{g}_0\| = 1$. In contrast to the aortic wall, neither collagenous nor elastic fibers are found in the ILT according to [63]. However, the differences between the thick and thin bundles of the fibrin network and the deposit of small condensed proteins might be possible explanations for anisotropy (cf., [63]). Since the behavior of the ILT material in compression remains unknown, it is assumed that the anisotropic response in (2.9) only contributes to the SEF if the material is in tension, i.e., $\bar{I}_4 > 1$ or $\bar{I}_6 > 1$. In analogy to the SEF for the aortic wall, also this constitutive equation degenerates to the material model presented in [24] for $\rho = 1$, whereas for $\rho = 0$ an isotropic model similar to [10] is obtained.

The phenomenological principal directions of anisotropy $\mathbf{a}_0$ and $\mathbf{g}_0$ in the reference configuration are again assumed to be symmetrically oriented with respect to the circumferential direction of the ILT and hence uniquely defined by the structural parameter ϕ, the in plane angle with respect to the local circumferential direction. Table 2.2 provides model parameters μ, k_1, k_2, ϕ and ρ for the luminal (anisotropic), the medial, and the abluminal layers of the ILT determined from a total number of 43 AAA samples (mean age 67.0 ± 6 yr), where 33 luminal, 22 medial and 12 abluminal layers have been tested and analyzed [63].

2.4 Definition of Fiber/Anisotropy Directions

The anisotropic constitutive models given in (2.6) and (2.9) for the AAA wall and the ILT, respectively, require the definition of the mean preferred directions $\mathbf{a}_0$ and $\mathbf{g}_0$ in the reference configuration as an input. Definition of these directions in patient-specific geometries,

however, is not a trivial task and requires a robust numerical algorithm to identify the local coordinate system at a specific location within the FE mesh. In the past, several methods have been presented which are either based on a highly structured FE mesh [44] or specific (predefined) tangential planes [33]. Nevertheless, the definition of preferred directions should be independent of any prerequisites and therefore a new algorithm is developed, applicable to both hexahedral and tetrahedral (with minor adjustments) FE meshes.

In order to obtain properly defined directions $\mathbf{a}_0^k$ and $\mathbf{g}_0^k$ for each element k in the FE mesh, an adequate assignment of the local radial, circumferential, and longitudinal directions needs to be performed (see Fig. 2.3). Thus, the AAA is divided into 3 different sections, the abdominal aorta section Ω_{AA}, the right common iliac Ω_{RI}, and the left common iliac Ω_{LI} artery section according to the present anatomical structure of the AAA, where the planes Γ_{t} (a transversal plane within the bifurcation) and Γ_{s} (a basically sagittal plane defined by the anterior, posterior, and caudal point introduced previously) are used. Subsequently unit direction vectors $\mathbf{n}_{\mathrm{avg}}^i$, with $i \in [\mathrm{AA, RI, LI}]$, of all individual sections are calculated using corresponding lumen centers at the top and the bottom of each section, defining their average orientation in space. In hexahedral FE meshes the definition of the radial direction for every element, independent of its individual size and shape, can be performed by calculation of two tangential planes ${}^{\mathrm{i}}\Gamma^k$ (inner element face) and ${}^{\mathrm{o}}\Gamma^k$ (outer element face), obtained via an orthogonal distance regression. These optimization problems are solved by minimizing the orthogonal (perpendicular) distances of the corresponding nodes at the element faces to the planes, leading to the unit normal vectors ${}^{\mathrm{i}}\mathbf{n}^k$ and ${}^{\mathrm{o}}\mathbf{n}^k$ of ${}^{\mathrm{i}}\Gamma^k$ and ${}^{\mathrm{o}}\Gamma^k$, respectively. Vector averaging retrieves

$$\mathbf{e}_{\mathrm{r}}^k = \frac{{}^{\mathrm{i}}\mathbf{n}^k + {}^{\mathrm{o}}\mathbf{n}^k}{\|{}^{\mathrm{i}}\mathbf{n}^k + {}^{\mathrm{o}}\mathbf{n}^k\|}, \tag{2.10}$$

leading to the definition of the local radial direction $\mathbf{e}_{\mathrm{r}}^k$ in the element coordinate system. Application of the vector product $\mathbf{n}_{\mathrm{avg}}^i \times \mathbf{e}_{\mathrm{r}}^k$, yields the local circumferential direction $\mathbf{e}_{\theta}^k$. A second vector product $\mathbf{e}_{\mathrm{r}}^k \times \mathbf{e}_{\theta}^k$ defines the local longitudinal direction $\mathbf{e}_{\mathrm{z}}^k$ in the element coordinate system, representing a modified direction of $\mathbf{n}_{\mathrm{avg}}^i$, with $i \in [\mathrm{AA, RI, LI}]$. Thus, the three orthogonal basis vectors $\mathbf{e}_{\mathrm{r}}^k, \mathbf{e}_{\theta}^k$, and $\mathbf{e}_{\mathrm{z}}^k$ represent the local element coordinate system. The local orthogonal basis calculated for each finite element serves as the foundation to define the mean preferred directions of anisotropy. In addition, the angles ϕ provided in Tables 2.1 and 2.2 for the AAA wall and the ILT, respectively, are needed to fully characterize these materials with preferred directions according to

$$\mathbf{a}_0^k = \cos\phi\,\mathbf{e}_{\theta}^k + \sin\phi\,\mathbf{e}_{\mathrm{z}}^k \qquad \text{and} \qquad \mathbf{g}_0^k = -\cos\phi\,\mathbf{e}_{\theta}^k + \sin\phi\,\mathbf{e}_{\mathrm{z}}^k. \tag{2.11}$$

2.5 Simulation Boundary Conditions

In FE analysis the correct application of boundary conditions is of crucial importance. Especially in simulations of biological structures such as AAAs their identification is not
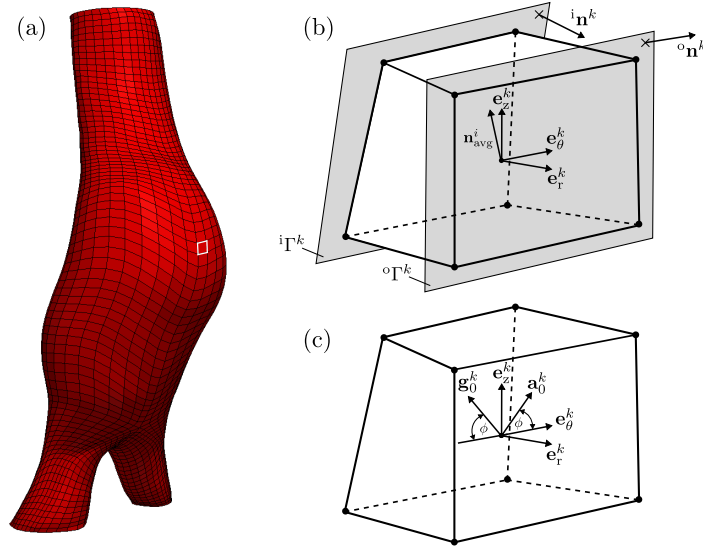
Figure 2.3: Method to define directions of anisotropy in (a) the structural discretization of the adventitia in the AAA wall; (b) enlarged schematic view on the indicated element with basis vectors $\mathbf{e}_r^k, \mathbf{e}_\theta^k$, and $\mathbf{e}_z^k$ of the local element coordinate system and (c) the mean directions of anisotropy are calculated using the average unit direction vector $\mathbf{n}_{avg}^i$.

trivial. Various boundary conditions on the patient-specific AAA geometry should reflect the *in vivo* situation, however, the FE model needs to be constrained for stable simulation conditions and convergence purposes. Boundary constraints should be chosen in a way so that their influence on simulation results is negligible or minimized. For the mathematical description of a boundary-value problem two specific types of boundary conditions, Dirichlet and Neumann boundary conditions, can be applied. In fact, there are also other types such as, e.g., Cauchy, Robin and mixed boundary conditions. In the following, Dirichlet and Neumann boundary conditions are treated separately and the application in the patient-specific FE model of the AAA is discussed.

Dirichlet Boundary Conditions.   Imposing a Dirichlet (geometrical) boundary condition to a PDE (the basic type of equation in FE stress analysis) specifies a distinct solution value at the boundary of the considered domain. In the context of FE analysis this means that displacements are applied $\mathbf{u}(\mathbf{X}) = \mathbf{u}$ or restricted $\mathbf{u}(\mathbf{X}) = \mathbf{0}$ at certain locations $\mathbf{X}$ in the reference configuration.

The AAA geometry reconstructed from MRI images represents the actual *in vivo* configuration in a patient. The length/height of the tissue composite does not change significantly during the cardiac cycle due to the pulse wave propagating through the aorta and the common iliac arteries. This fact justifies fixing all nodes in vertical direction at the cranial edge

(transition zone of the AAA to the connected part of the abdominal aorta) and the caudal edges (transition zones of the AAA to the common iliac arteries) of the AAA geometry. As already mentioned in the introduction, the human abdominal aorta is an elastic artery being quite distensible, necessary to take up the pulsatile nature of blood pressure. As the pressure wave propagates through the aorta it expands in radial direction. Thus, displacements of nodes at the three different transition zones intersecting with the lumen surface are constrained in circumferential direction and can only move in local radial direction (radially along the direction of the lumen center to the individual node).

Neumann Boundary Conditions. Mathematically, a Neumann (natural) boundary condition provides a value for the derivative of the solution of a PDE on the boundary of the considered domain. In the context of FE analysis this could be a traction vector $\mathbf{t}(\mathbf{X})$ acting on a certain location $\mathbf{X}$ in the reference configuration.

The AAA of the patient undergoing MRI is subjected to physiological *in vivo* conditions, i.e., to systolic (optimal < 120 mmHg) or diastolic (optimal < 80 mmHg) blood pressure depending on the imaging procedure [67]. However, since AAA formation is a pathological process the patient is assumed to have a diastolic blood pressure (DBP) of $p = 85$ mmHg and a systolic blood pressure (SBP) of $p = 135$ mmHg ('Prehypertension' according to [7]). Increasing pressurization in the process of FE simulations leads to changes in the geometry due to the finite elasticity of the biological tissue. Since pressure acts perpendicular to the surface considered, the direction of the load associated with the applied pressure changes during FE analysis, leading to a follower load applied on the lumen boundary surface. Depending on the direction of the luminal surface normal (inward or outward), the adequate sign of the applied pressure needs to be selected.

2.6 Methodology for Residual Stretch/Stress

Numerous problems arise from the inclusion of residual stresses/stretches into patient-specific simulations of arterial tissue since classical FE approaches assume an unloaded and stress-free reference configuration. In the past several methods have been introduced to account for residual stresses in a patient-specific FE model of a human iliac artery or a human thoracic aorta [1,3,70]. However, analyses are either based on a single experimentally-determined (two-dimensional) so-called 'opening angle' (cf., e.g., [15]) or on layer-specific uniform residual stretches, both not being able to represent the three-dimensional nature of residual stresses in arteries. In the following, an approach is presented capable to include layer-specific three-dimensional residual stretches (and hence residual stresses) based on an analytical analysis into patient-specific FE simulations of AAAs. The general idea of the method developed is applicable to any residually stressed tissue where adequate data on residual deformations are available. The method is based on a recent analytical approach to determine residual stresses [25], in which experimental data of human abdominal aortas with non-atherosclerotic intimal thickening are used [26].

2.6.1 Analytic Residual Stretch Calculation

In order to estimate residual stretches in patient-specific AAA geometries, deformation gradients $\mathbf{F}^{(i)}(r^{(i)})$, with $i \in [\mathrm{I}, \mathrm{M}, \mathrm{A}]$, for the intima, media, and adventitia, respectively, are defined as a function of the radius $r^{(i)}$ in the residually stressed configuration. They represent the kinematic transformation of the individual arterial layers from their (nearly) stress-free reference configuration into a circular cylindrical tube, in which any external load is absent (cf., [25]). Due to the discrete nature of the FE mesh every element in the AAA geometry is assumed to undergo one of these deformations depending on the spatial location within the arterial layer.

Deformation Gradient in the Intima.   Measurements in [26] indicate that the intima basically remains straight in axial direction, whereas an aortic ring (circumferential direction) opens up by a distinct amount. Under these assumptions the deformation gradient for the intima can be specified as

$$
\begin{aligned}
\mathbf{F}^{(\mathrm{I})}(r^{(\mathrm{I})}) \;=\; & \frac{L^{(\mathrm{I})}}{r^{(\mathrm{I})}k^{(\mathrm{I})}l}[A^{(\mathrm{I})2} + k^{(\mathrm{I})}\frac{l}{L^{(\mathrm{I})}}(r^{(\mathrm{I})2} - a^{(\mathrm{I})2})]^{(1/2)}\mathbf{e}_r \otimes \mathbf{E}_R \\
& + \frac{r^{(\mathrm{I})}k^{(\mathrm{I})}}{[A^{(\mathrm{I})2} + k^{(\mathrm{I})}\frac{l}{L^{(\mathrm{I})}}(r^{(\mathrm{I})2} - a^{(\mathrm{I})2})]^{(1/2)}}\mathbf{e}_\theta \otimes \mathbf{E}_\Theta \\
& + \frac{l}{L^{(\mathrm{I})}}\mathbf{e}_z \otimes \mathbf{E}_Z .
\end{aligned}
\tag{2.12}
$$

Deformation Gradient in the Media.   According to [26] the media exhibits pronounced curvatures after layer separation in both longitudinal and circumferential direction. For simplicity and practicability of the analytical analysis it is assumed that the aortic tissue is planar in the direction of the smaller curvature, i.e., in circumferential direction (cf., [25]). Therefore, the kinematic transformation including a minor adjustment factor $c^{(\mathrm{M})}$ is given by

$$
\begin{aligned}
\mathbf{F}^{(\mathrm{M})}(r^{(\mathrm{M})}) \;=\; & \frac{L^{(\mathrm{M})}\pi}{c^{(\mathrm{M})}r^{(\mathrm{M})}\beta l^{(\mathrm{M})}k^{(\mathrm{M})}}[A^{(\mathrm{M})2} + \frac{\beta l^{(\mathrm{M})}k^{(\mathrm{M})}}{\pi L^{(\mathrm{M})}}(b^{(\mathrm{M})2} - r^{(\mathrm{M})2})]^{(1/2)}\mathbf{e}_r \otimes \mathbf{E}_R \\
& + \frac{r^{(\mathrm{M})}\beta}{c^{(\mathrm{M})}L^{(\mathrm{M})}}\mathbf{e}_\theta \otimes \mathbf{E}_Z \\
& + \frac{c^{(\mathrm{M})2}l^{(\mathrm{M})}k^{(\mathrm{M})}}{\pi[A^{(\mathrm{M})2} + \frac{\beta l^{(\mathrm{M})}k^{(\mathrm{M})}}{\pi L^{(\mathrm{M})}}(b^{(\mathrm{M})2} - r^{(\mathrm{M})2})]^{(1/2)}}\mathbf{e}_z \otimes \mathbf{E}_\Theta .
\end{aligned}
\tag{2.13}
$$

Deformation Gradient in the Adventitia.   Observations in [26] indicate that the axial strips of the adventitia essentially do not undergo any deformation, they remain straight.

intima	media	adventitia
$A^{(\mathrm{I})} = 7.504\,\mathrm{mm}$	$A^{(\mathrm{M})} = 8.406\,\mathrm{mm}$	$L_1^{(\mathrm{A})} = 0.205\,\mathrm{mm}$
$B^{(\mathrm{I})} = 7.764\,\mathrm{mm}$	$B^{(\mathrm{M})} = 8.986\,\mathrm{mm}$	$L_2^{(\mathrm{A})} = 18.3465\,\mathrm{mm}$
$L^{(\mathrm{I})} = 2.5805\,\mathrm{mm}$	$L^{(\mathrm{M})} = 2.52\,\mathrm{mm}$	$L_3^{(\mathrm{A})} = 2.288\,\mathrm{mm}$
$k^{(\mathrm{I})} = 1.191$	$k^{(\mathrm{M})} = 2.785$	
$a^{(\mathrm{I})} = 5.61\,\mathrm{mm}$	$a^{(\mathrm{M})} = 5.911\,\mathrm{mm}$	$a^{(\mathrm{A})} = 6.724\,\mathrm{mm}$
$b^{(\mathrm{I})} = 5.91\,\mathrm{mm}$	$b^{(\mathrm{M})} = 6.724\,\mathrm{mm}$	$b^{(\mathrm{A})} = 7.045\,\mathrm{mm}$
$l = 2.48\,\mathrm{mm}$	$l = 2.48\,\mathrm{mm}$	$l = 2.48\,\mathrm{mm}$
$\mu^{(\mathrm{I})} = 39.8\,\mathrm{kPa}$	$\mu^{(\mathrm{M})} = 31.4\,\mathrm{kPa}$	$\mu^{(\mathrm{A})} = 17.3\,\mathrm{kPa}$

Table 2.3: Geometrical parameters determined from experiments used for calculation of the deformation gradients $\mathbf{F}^{(i)}(r^i)$, with $i \in [\mathrm{I, M, A}]$, for the individual arterial tissue layers [26] and associated material parameters [23].

However, circumferential strips of aortic rings spring open and form a plane, leading to the kinematic transformation

$$
\begin{aligned}
\mathbf{F}^{(\mathrm{A})}(r^{(\mathrm{A})}) \;=\; & \frac{L_2^{(\mathrm{A})} L_3^{(\mathrm{A})}}{\pi r^{(\mathrm{A})} l} \mathbf{e}_r \otimes \mathbf{E}_{X_1} \\
& + \frac{\pi r^{(\mathrm{A})}}{L_2^{(\mathrm{A})}} \mathbf{e}_\theta \otimes \mathbf{E}_{X_2} \\
& + \frac{l}{L_3^{(\mathrm{A})}} \mathbf{e}_z \otimes \mathbf{E}_{X_3}.
\end{aligned}
\tag{2.14}
$$

The deformation gradients provided in (2.12)-(2.14) representing the underlying kinematic transformation are functions of the radii $r^{(i)} \in [a^{(i)}, b^{(i)}]$, with $i \in [\mathrm{I, M, A}]$. In addition, since the cylindrical polar coordinate axes in the current configuration are principal axes, the deformation gradients only have diagonal entries $\lambda_r^{(i)}$, $\lambda_\theta^{(i)}$, and $\lambda_z^{(i)}$, denoting the principal stretches, again with $i \in [\mathrm{I, M, A}]$. The deformation of each individual layer is assumed to be isochoric, i.e., the material is treated as incompressible. Thus, the condition

$$
\lambda_r^{(i)} \lambda_\theta^{(i)} \lambda_z^{(i)} = 1, \qquad \text{with} \qquad i \in [\mathrm{I, M, A}],
\tag{2.15}
$$

is fulfilled. It is important to emphasize that all parameters in (2.12)-(2.14), except $l^{(\mathrm{M})}$ and β discussed in the following, are geometrical measures obtained directly from experiments as specified in Table 2.3. In order to evaluate presented deformation gradients and thus the principal stretches in every individual layer, traction continuity for stresses in radial direction is enforced at the interfaces between the intima and the media as well as between

the media and the adventitia [25]. Additionally, making use of the geometric relation

$$l^{(\mathrm{M})} = \frac{\pi L^{(\mathrm{M})}}{\beta k^{(\mathrm{M})}} \frac{(B^{(\mathrm{M})^2} - A^{(\mathrm{M})^2})}{(b^{(\mathrm{M})^2} - a^{(\mathrm{M})^2})} \tag{2.16}$$

between the remaining unknown geometrical parameters $l^{(\mathrm{M})}$ and β, an analytical expression for β can be determined. Thus,

$$
\begin{aligned}
\beta = {} & \left[\frac{\mu^{(\mathrm{M})}(b^{(\mathrm{M})^2} - a^{(\mathrm{M})^2})}{L^{(\mathrm{M})^2}} \right]^{-1/2} \\
& \times \left[\frac{\mu^{(\mathrm{I})}L^{(\mathrm{I})}(b^{(\mathrm{I})^2} - a^{(\mathrm{I})^2})(A^{(\mathrm{I})^2}L^{(\mathrm{I})} - l a^{(\mathrm{I})^2}k^{(\mathrm{I})})}{l^2 a^{(\mathrm{I})^2} b^{(\mathrm{I})^2} k^{(\mathrm{I})^2}} \right. \\
& + \frac{2\mu^{(\mathrm{I})}L^{(\mathrm{I})} \left(\log\left[\frac{b^{(\mathrm{I})}}{a^{(\mathrm{I})}} \right] - k^{(\mathrm{I})^2}\log\left[\sqrt{1 + \frac{l k^{(\mathrm{I})}(b^{(\mathrm{I})^2} - a^{(\mathrm{I})^2})}{L^{(\mathrm{I})}A^{(\mathrm{I})^2}}} \right] \right)}{l k^{(\mathrm{I})}} \\
& + \frac{\mu^{(\mathrm{M})}(b^{(\mathrm{M})^2} - a^{(\mathrm{M})^2})^2(b^{(\mathrm{M})^2}B^{(\mathrm{M})^2} - a^{(\mathrm{M})^2}A^{(\mathrm{M})^2})}{a^{(\mathrm{M})^2}b^{(\mathrm{M})^2}(B^{(\mathrm{M})^2} - A^{(\mathrm{M})^2})^2} \\
& - \frac{2\mu^{(\mathrm{M})}(b^{(\mathrm{M})^2} - a^{(\mathrm{M})^2})\log\left[\frac{b^{(\mathrm{M})}}{a^{(\mathrm{M})}} \right]}{B^{(\mathrm{M})^2} - A^{(\mathrm{M})^2}} \\
& \left. + \mu^{(\mathrm{A})}(b^{(\mathrm{A})^2} - a^{(\mathrm{A})^2}) \left(\frac{L_2^{(\mathrm{A})^2}L_3^{(\mathrm{A})^2}}{\pi^2 l^2 a^{(\mathrm{A})^2}b^{(\mathrm{A})^2}} - \frac{\pi^2}{L_2^{(\mathrm{A})^2}} \right) \right]^{1/2} ,
\end{aligned}
\tag{2.17}
$$

where $\mu^{(\mathrm{I})}$, $\mu^{(\mathrm{M})}$, and $\mu^{(\mathrm{A})}$ denote the experimentally-determined shear moduli of the arterial layers (intima, media, and adventitia, respectively) fitted to the low load regime (up to the so-called 'transition-point') in [23].

2.6.2 Pragmatic Mapping of Residual Stretch

In order to incorporate the three-dimensional residual stresses/stretches in FE simulations of AAAs, the analytically estimated residual stretches from (2.12)-(2.14) are mapped into a predefined element-specific orthonormal coordinate basis (see Section 2.4) for every Gauss quadrature point depending on the location within each tissue layer. The proposed mapping procedure is applicable to both tetrahedral (with minor modifications) as well as structured and unstructured hexahedral meshes.

For every Gauss integration point j ($j = 1, 2, \ldots, n$; where n is the total number of Gauss quadrature points in the FE model) in each element within each arterial tissue layer i ($i \in [\mathrm{I}, \mathrm{M}, \mathrm{A}]$), the 'regional' radial direction of the AAA tissue layer is defined by a vector $\bar{\mathbf{n}}_j^{(i)}$, which in general differs from the radial direction $\mathbf{e}_\mathrm{r}^k$ of the local coordinate system in
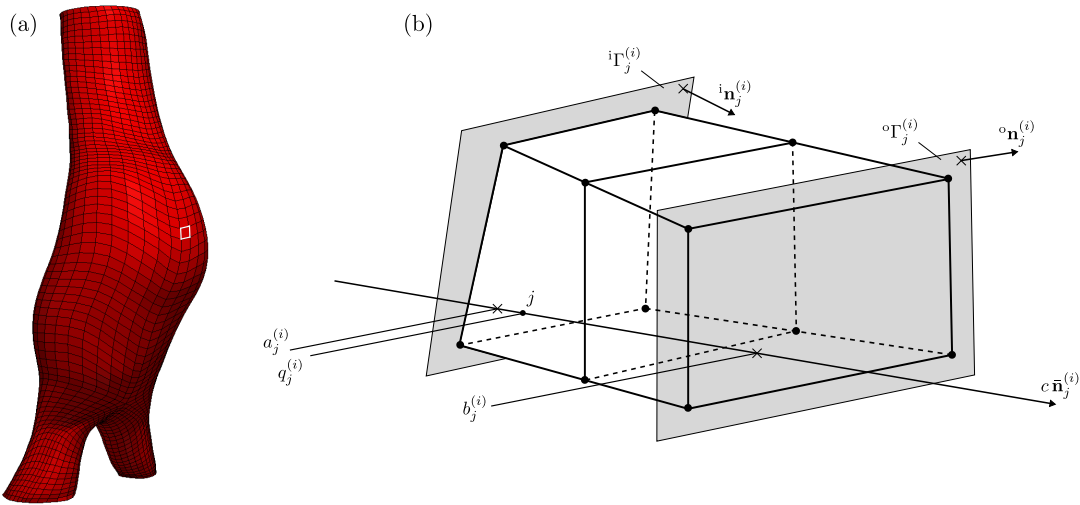
Figure 2.4: Representative schematic diagram of the vector in the 'regional' radial direction passing through Gauss integration point j, $c\bar{\mathbf{n}}_j^{(i)}$: (a) patient-specific FE mesh of the adventitia with selected elements, (b) perspective view of elements comprising the adventitia as the representative tissue layer i indicating the performed approach.

element k (see Fig. 2.4), though the difference might be small. To calculate the 'regional' radial direction for the Gauss quadrature point j in the arterial tissue layer i, the four nodes defining the hexahedral element at the inner edge of the tissue layer, e.g., the intersection surface of media and adventitia, are determined. Using orthogonal distance regression a plane is fitted to these four nodal points, leading to the unit normal vector $^{\mathrm{i}}\mathbf{n}_j^{(i)}$ of this inner plane. This process is repeated for the same Gauss integration point j, determining the four nodes of the hexahedral element at the outer surface of the arterial tissue layer, e.g., the outer edge of the AAA wall. Again, a plane is fitted using orthogonal distance regression to determine the unit normal vector $^{\mathrm{o}}\mathbf{n}_j^{(i)}$ of this outer plane. Finally, the average of both is calculated, representing the 'regional' radial direction of the AAA tissue layer given as

$$\bar{\mathbf{n}}_j^{(i)} = \frac{^{\mathrm{i}}\mathbf{n}_j^{(i)} + {}^{\mathrm{o}}\mathbf{n}_j^{(i)}}{\|^{\mathrm{i}}\mathbf{n}_j^{(i)} + {}^{\mathrm{o}}\mathbf{n}_j^{(i)}\|}, \tag{2.18}$$

where Einstein summation convention is not employed. The subsequent step includes the calculation of a vector $c\bar{\mathbf{n}}_j^{(i)}$, where $c \in \mathbb{R}_+^*$ is sufficiently large, defined to pass through Gauss quadrature point j (see Fig. 2.4 for a schematic representation). Along this 'regional' radial direction vector $c\bar{\mathbf{n}}_j^{(i)}$ three associated distances (locations) are calculated using an arbitrarily defined starting point towards the lumen center: $a_j^{(i)}$ is the distance at

the intersection of $c\,\bar{\mathbf{n}}_j^{(i)}$ with the inner plane having the unit normal $^{\mathrm{i}}\mathbf{n}_j^{(i)}$, denoted by $^{\mathrm{i}}\Gamma_j^{(i)}$; $q_j^{(i)}$ is the distance of Gauss quadrature point j along $c\,\bar{\mathbf{n}}_j^{(i)}$ within tissue layer i; and $b_j^{(i)}$ is the distance at the intersection of $c\,\bar{\mathbf{n}}_j^{(i)}$ with the outer plane having the unit normal $^{\mathrm{o}}\mathbf{n}_j^{(i)}$, denoted by $^{\mathrm{o}}\Gamma_j^{(i)}$. Aforementioned definitions for the Gauss integration point j within the arterial tissue layer i along the vector $c\,\bar{\mathbf{n}}_j^{(i)}$ lead to $a_j^{(i)} \leq q_j^{(i)} \leq b_j^{(i)}$.

Identification of the position of the Gauss quadrature point j with respect to the thickness of the arterial tissue layer i requires the definition of a 'normalized' distance, given as

$$f_j^{(i)} = \frac{q_j^{(i)} - a_j^{(i)}}{b_j^{(i)} - a_j^{(i)}}, \tag{2.19}$$

where $f_j^{(i)} \in [0,1]$. Finally, the three-dimensional residual stretches for Gauss quadrature point j in arterial tissue layer i are determined using (2.12)-(2.14) evaluated with

$$r_j^{(i)} = a^{(i)} + f_j^{(i)}(b^{(i)} - a^{(i)}), \tag{2.20}$$

where $a^{(i)}$ and $b^{(i)}$ ($i \in [\mathrm{I}, \mathrm{M}, \mathrm{A}]$) are given in Table 2.3. This procedure is repeated for all Gauss integration points j in all arterial tissue layers i of the FE mesh. Note that the 'regional' radial vector $\bar{\mathbf{n}}_j^{(i)}$ and thus also the modified version $c\,\bar{\mathbf{n}}_j^{(i)}$ is the same for every Gauss point j within an element k. However, depending on the orientations of the fitted inner $^{\mathrm{i}}\Gamma_j^{(i)}$ and outer plane $^{\mathrm{o}}\Gamma_j^{(i)}$ in space, the distances $a_j^{(i)}$, $q_j^{(i)}$ and $b_j^{(i)}$ differ, leading to a variation of the 'normalized' distance $f_j^{(i)}$.

The procedure described above provides a pragmatic approach to map analytically determined residual stretches at each Gauss quadrature point j in arterial tissue layer i into an element-specific orthonormal cylindrical coordinate basis defined by unit vectors $\mathbf{e}_{\mathrm{r}}^k, \mathbf{e}_{\theta}^k$, and $\mathbf{e}_{\mathrm{z}}^k$. However, FE simulations are based on a global Cartesian coordinate system ($\mathbf{e}_{\mathrm{x}}, \mathbf{e}_{\mathrm{y}}$, and $\mathbf{e}_{\mathrm{z}}$), thus, the deformation gradients calculated by (2.12)-(2.14) need to be transformed. The three-dimensional transformation of any tensor quantity such as the deformation gradients $\mathbf{F}^{(i)}(r^{(i)})$ from a rotated orthonormal right-handed coordinate basis into the global orthonormal right-handed FE coordinate basis is performed by

$$\mathbf{F}_{\mathrm{RS}}^{(i)} = \mathbf{Q}^{\mathrm{T}}\mathbf{F}^{(i)}\mathbf{Q}, \tag{2.21}$$

where $\mathbf{Q}$ denotes the proper orthogonal rotation matrix, i.e., having the properties $\det\mathbf{Q} = +1$, $\mathbf{Q}^{\mathrm{T}}\mathbf{Q} = \mathbf{I}$, and $\mathbf{Q}^{-1} = \mathbf{Q}^{\mathrm{T}}$. The components of the rotation matrix $\mathbf{Q}$ are denoted as the direction cosines retrieved by $Q_{ij} = \mathbf{e}_i \cdot \mathbf{e}_j$, where $i = \mathrm{r}, \theta, \mathrm{z}$ and $j = \mathrm{x}, \mathrm{y}, \mathrm{z}$, representing unit direction vectors in the rotated cylindrical element coordinate system and the global Cartesian coordinate system, respectively.

2.6.3 Computational Implementation of Residual Stretch

In previous sections analytical procedures for the definition of the directions of anisotropy (fiber directions) in the reference configuration, the estimation of residual stretches in arterial tissue layers based on experimental results, as well as a methodology to map these residual stretches into patient-specific FE geometries have been provided and discussed. These approaches serve as the mathematical basis for computational preprocessing to perform FE simulations of AAAs. Two problems arise when classical FE simulations of arteries are performed: (i) the imaged *in vivo* geometry is not an unloaded reference configuration, it is subjected to *in vivo* boundary conditions, e.g., DBP, and (ii) the influence of residual stresses is modeled in an insufficient way or, even worse, totally neglected. In the following, the computational implementation addressing both problems, the inclusion of the three-dimensional residual stretches as well as to account for *in vivo* boundary conditions, in the multipurpose FE code FEAP (University of California, Berkeley, CA) is discussed. A representative schematic providing an overview of the individually performed simulation steps is provided in Fig. 2.5. Note that residual stressing is performed prior to prestressing, conversely to what is performed in experiments (the artery is extracted from the patient (unloaded) and afterwards residual stress experiments are performed). This fact is important since material non-linearity influences deformation and hence stress calculation.

Residual Stressing of Abdominal Aortic Aneurysms. In Sections 2.6.1 and 2.6.2 methods to calculate, to map and to transform the estimated residual stretches $\mathbf{F}_{\mathrm{RS}}^{(i)}$, with $i \in [\mathrm{I}, \mathrm{M}, \mathrm{A}]$, at each Gauss quadrature point j for every arterial tissue layer i in the patient-specific FE model of the considered AAA have been provided. So far, residual stresses in the ILT, which is present in the majority of AAAs [63], are not considered at all. However, observations in the laboratory of the Institute of Biomechanics at Graz University of Technology suggest, that residual stresses in the individual layers of the ILT are small. Thus, it is assumed that they are negligible and therefore not included in FE analysis, i.e., $\mathbf{F}_{\mathrm{RS}}^{(\mathrm{T})} = \mathbf{I}$, where $\mathbf{I}$ is the second-order identity tensor.

The classical FE method assumes the reference configuration to be unloaded and stress-free. Inclusion of residual stretches at every Gauss integration point j in every arterial tissue layer i will result in stresses and perturbation of the global equilibrium in the FE model. This fact might lead to a non-converged solution or to no solution at all, depending on the magnitude of perturbation of the global equilibrium. In order to overcome this problem, a so-called 'tissue scaffold' for the AAA geometry is introduced, essentially a continuum body Ω_{scaf} having an identical geometry and sharing the same nodes in the FE mesh as the imaged *in vivo* configuration Ω_{IV}. However, for the elements associated with the 'tissue scaffold', denoted as 'ghost' elements, an isotropic material model is used for simplicity. Again, the decomposition of the SEF (see (1.33)) into an isochoric and a
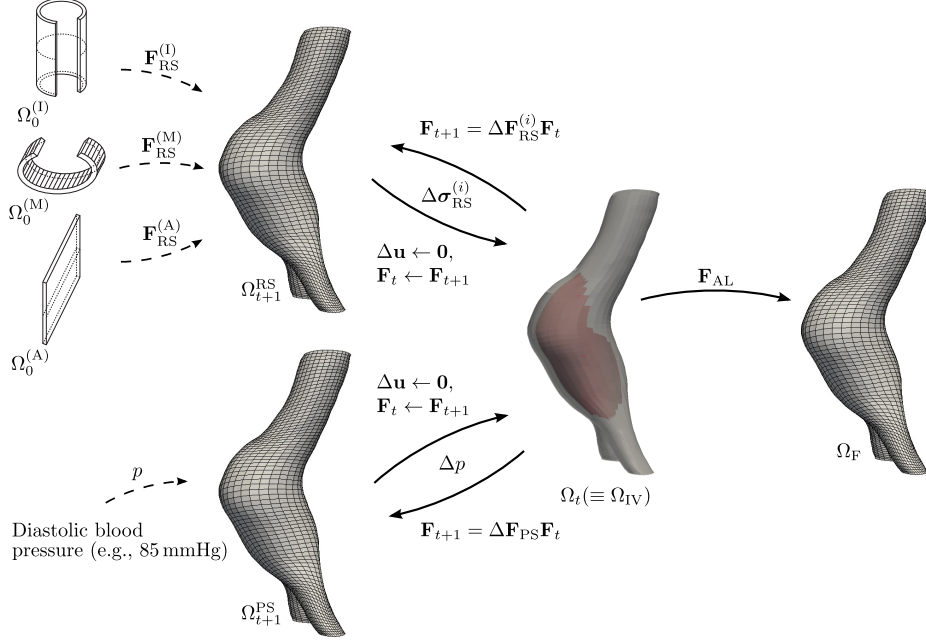
Figure 2.5: Representative schematic of the computational implementation addressing the two major problems in FE simulations of AAA, the inclusion of residual stretches and the application of *in vivo* boundary conditions onto the imaged patient-specific FE model.

volumetric contribution is performed, where the latter is particularized as

$$\Psi_{\mathrm{vol}}^{\mathrm{scaf}}(J) = \frac{\mu_{\mathrm{K}}^{\mathrm{scaf}}}{2}(J-1)^2, \tag{2.22}$$

in which $\mu_{\mathrm{K}}^{\mathrm{scaf}}$ defines the arbitrarily chosen bulk modulus. The isochoric part of the constitutive model describing the mechanical behavior of the 'ghost' elements and hence the 'tissue scaffold' is given by

$$\Psi_{\mathrm{iso}}^{\mathrm{scaf}}(\bar{I}_1) = \frac{\mu_{\mathrm{scaf}}}{2}(\bar{I}_1 - 3), \tag{2.23}$$

where μ_{scaf} is a stress-like material parameter, the shear modulus in the reference configuration, initially assumed to be very large (in the range of several MPa, i.e., $\mu_{\mathrm{scaf}} >> \mu$). The high stiffness of the 'tissue scaffold' supports the actual FE mesh of the AAA geometry after inclusion of the residual stretches, keeping the nodes in place and allowing only for small displacements. Thus, a converged FE solution in equilibrium with applied boundary conditions can be obtained. Subsequently the initial shear modulus μ_{scaf} is gradually decreased in every time step, allowing for larger deformations in the AAA geometry until the stiffness of the 'tissue scaffold' vanishes and residual stretches are in equilibrium with the

boundary conditions. In order to obtain the *in vivo* configuration Ω_{IV} with associated nodal coordinates $\mathbf{x}_t$ after residual stretches are included, a Generalized Prestressing Algorithm (GPA) presented in [68] and based on the concept of [18, 19] denoted to as the Modified Updated Lagrangian Formulation (MULF), is applied (see upper left section in Fig. 2.5). For this purpose, an incremental deformation gradient

$$\Delta\mathbf{F}_{\mathrm{RS}}^{(i)} = \mathbf{I} + \frac{\partial\Delta\mathbf{u}}{\partial\mathbf{x}_t} \tag{2.24}$$

is calculated as a result of the incremental displacements $\Delta\mathbf{u}$ (representing the associated deformation) enforced by the residual stretches $\mathbf{F}_{\mathrm{RS}}^{(i)}$ due to the relaxation of the 'tissue scaffold' for each iteration step. Subsequently the deformation gradient in the current time step is computed as $\mathbf{F}_{t+1} = \Delta\mathbf{F}_{\mathrm{RS}}^{(i)}\mathbf{F}_t$, where $\mathbf{F}_t$ is a general history term. Global equilibrium in the FE analysis is obtained in the current virtual configuration $\Omega_{t+1}^{\mathrm{RS}}$, which differs from the imaged configuration Ω_{IV} (magnitude of mismatch is dependent on the number of time steps used). Consecutively the deformation increment $\Delta\mathbf{u}$ is deleted to retain the *in vivo* geometry and the deformation history is updated during computation by $\mathbf{F}_{t+1} = \mathbf{F}_t$, i.e., the current total deformation gradient, thus, building up a final deformation gradient without changing the imaged *in vivo* geometry.

Generalized Prestressing of Abdominal Aortic Aneurysms. The proposed GPA [68] is a multifunctional tool for including various types of boundary conditions in FE analyses without changing the geometry, and is used in the following to include the blood pressure during MRI, e.g., $p = 85\,\mathrm{mmHg}$ (see lower left section in Fig. 2.5). Blood pressure measurement has not been performed during medical imaging and is therefore estimated according to clinical advice. Similar to what is performed during inclusion of residual stretches/stresses, an incremental deformation gradient is calculated for every time step as

$$\Delta\mathbf{F}_{\mathrm{PS}} = \mathbf{I} + \frac{\partial\Delta\mathbf{u}}{\partial\mathbf{x}_t}, \tag{2.25}$$

where the incremental displacement $\Delta\mathbf{u}$ results from the application of an internal pressure increment Δp. Again the deformation gradient in the current time step is calculated by $\mathbf{F}_{t+1} = \Delta\mathbf{F}_{\mathrm{PS}}\mathbf{F}_t$, where $\mathbf{F}_t$ is a general history term stored during computation. Global equilibrium in the FE analysis is achieved in the current virtual configuration $\Omega_{t+1}^{\mathrm{PS}}$, different from the aforementioned virtual configuration $\Omega_{t+1}^{\mathrm{RS}}$. In order to obtain the imaged *in vivo* geometry after application of the total blood pressure p, the deformation increment $\Delta\mathbf{u}$ is deleted and the deformation history is updated as $\mathbf{F}_{t+1} = \mathbf{F}_t$, thus, building up a final deformation gradient maintaining the imaged *in vivo* geometry and including now both residual stretches/stresses and blood pressure.

Stress Analysis on Physiological Conditions. Sequential performance of the residual stretching/stressing (inclusion of residual stretches/stresses in the AAA) and the prestressing (inclusion of blood pressure in the AAA) algorithms discussed so far, incorporates all

essential *in vivo* boundary conditions by maintaining the imaged configuration Ω_{IV}. These procedures serve as the basis to investigate different physiological and pathophysiological loading conditions within the patient-specific AAA geometry, which can be modeled by subsequent application of various arbitrary loads, leading to $\mathbf{F}_{\mathrm{AL}}$ and different configurations Ω_{F} (see right section in Fig. 2.5). It is assumed that investigated patients have a DBP of $p = 85$ mmHg (blood pressure at which medical imaging is performed) and the SBP is estimated to be $p = 135$ mmHg. Thus, the convenient medical measure of the mean arterial pressure (MAP), which approximates the average arterial blood pressure of a patient during a single cardiac cycle, defined as

$$\mathrm{MAP} = \mathrm{DBP} + \frac{1}{3}(\mathrm{SBP} - \mathrm{DBP}) \tag{2.26}$$

is calculated to be 101.67 mmHg. The assumed blood pressures correspond to so-called 'Prehypertension', which might be consistent with the fact that AAA formation is a pathological process [67]. It is important to emphasize that blood pressure is estimated under normal resting conditions. It is reported, that peak pressures of a single subject measured in the left brachial artery may exceeded 480 mmHg and 350 mmHg for SBP and DBP under heavy resistance exercise (double-leg press) [41].

2.7 Validation of Residual Stretch/Stress

Assumptions as well as the proposed FE framework for including residual stretches/stresses into patient-specific models of AAAs are validated by numerical reconstruction of a right circular cylinder tube and compared to the analytical solution in [25]. Therefore, the three individual layers (intima, media, and adventitia) of a human abdominal aorta are modeled in their (nearly) stress-free reference configuration and numerically reconstructed via the FE method to form a right circular cylinder tube, which represents an idealized geometry of the type of artery under consideration. Because of symmetry conditions only an eighth of the tube is modeled, similar to a longitudinal aortic strip in [26].

It is unlikely that residual deformations can be characterized appropriately by a single two-dimensional parameter such as the 'opening angle' due to the inhomogeneous nature of the arterial wall [26]. The novelty of the study presented in [26] concerns the fact that they defined the three-dimensional residual deformations of every individual arterial layer by stretches and curvatures in both axial and circumferential direction. Hence, the very complex geometry of the (nearly) stress-free reference configurations of all individual layers is approximated and modeled by subareas of either a right circular cylinder or a torus surface, superimposed to form a three-dimensional FE mesh. The general mathematical description, i.e., the parametric equation, of a right circular cylinder in the global Cartesian coordinate system used in this validation is given by

$$\mathbf{X}_{\mathrm{cyl}}(\theta) = \begin{bmatrix} h \\ R\cos\theta \\ R\sin\theta \end{bmatrix}, \tag{2.27}$$

	t_{ref} [mm]	λ_{axial} [-]	λ_{circ} [-]	c_{axial} [mm^{-1}]	c_{circ} [mm^{-1}]
intima	0.260	0.961	0.899	−0.009	0.131
media	0.580	0.490	1.454	−0.115	−0.032
adventitia	0.410	1.084	1.179	0.000	−0.003

Table 2.4: Mean values of the thickness t_{ref} and analytically determined residual stretches in axial λ_{axial} and circumferential direction λ_{circ} (evaluated at the center of every individual layer) in the (nearly) stress-free reference configuration for the aortic layers intima, media and adventitia taken from [25]. Mean axial c_{axial} and circumferential c_{circ} curvature of individual layers 6 h after layer separation and relaxation in a Ca^{2+}-free physiological saline solution to avoid muscle activation from [26].

where R denotes the radius of the right circular cylinder surface, θ is an angle in the range of $[0, 2\pi)$ and h is a parameter defining the longitudinal position, i.e., the height of the right circular cylinder surface. The parametric equation for the torus in the Cartesian coordinate system used is given by

$$\mathbf{X}_{tor}(\theta, \phi) = \begin{bmatrix} (R + r\cos\theta)\sin\phi \\ r\sin\theta \\ (R + r\cos\theta)\cos\phi \end{bmatrix}, \tag{2.28}$$

where r is the radius of a circle rotating around the torus axis at a circular orbit with radius R and θ and ϕ are parameters in the range of $[0, 2\pi)$. Depending on the relative size of both radii R and r, different classes of standard tori are obtained. If $R > r$ the surface represents a ring torus, however, if $R = r$ a horn torus is obtained. In the case of $R < r$ a self-intersecting spindle torus is parameterized, which degenerates into a sphere for $R = 0$. Using the parametric descriptions given in (2.27) and (2.28) allows to mimic the curvatures as well as the stretches in longitudinal and circumferential direction with acceptable accuracy. These parameters, as well as the individual layer thicknesses in the reference configuration, for the intima, the media, and the adventitia are provided in Table 2.4. Minor adjustments of parameterizations given in (2.27) and (2.28) for individual layers are necessary as discussed in the following.

Reference Geometry of the Intima. In this validation the intima is considered to have a significant contribution to the overall mechanical behavior of the modeled abdominal aorta since it has a considerable thickness in comparison to the other layers due to non-atherosclerotic intimal thickening [60]. According to the data in Table 2.4, the intima is in compression in axial and circumferential direction in the unloaded idealized state, leading to an elongation after layer separation in the experiment. In addition to that, it has two significant curvatures, a negative one in the axial and a positive one in the circumferential direction, which can be modeled via sections of the inner surface of a torus. Since a closed

mathematical description of an area on the torus surface having constant width and length does not exist and axial dimensions are predominant in the example given, (2.28) needs to be modified that the axial length of the intima strip is constant over the entire circumferential dimension. Therefore, a parameter transformation of $\phi = \phi(\bar{\phi}, \theta)$ is performed using the scaling factor

$$f^{(\mathrm{I})}(\theta) = \frac{R + r\cos\theta}{R - r}, \tag{2.29}$$

where $f^{(\mathrm{I})}(\theta) \geq 1$. The introduced scaling factor transforms the rotation angle according to $\phi(\bar{\phi}, \theta) = \bar{\phi}/f^{(\mathrm{I})}(\theta)$ and hence (2.28) can be rewritten as

$$\mathbf{X}^{(\mathrm{I})}(\theta, \phi) = \begin{bmatrix} (R + r\cos\theta)\sin(\bar{\phi}/f^{(\mathrm{I})}(\theta)) \\ r\sin\theta \\ (R + r\cos\theta)\cos(\bar{\phi}/f^{(\mathrm{I})}(\theta)) \end{bmatrix}. \tag{2.30}$$

This parametric equation defines a surface used to approximate the intima in the (nearly) stress-free configuration. Superposition of four surfaces leads to the definition of three individual layers of linear hexahedral elements through the thickness. The (nearly) stress-free reference configuration of the intima is shown in Fig. 2.6 and denoted by $\Omega_0^{(\mathrm{I})}$.

Reference Geometry of the Media. The media is generally considered to be the most important layer in arterial wall mechanics having a large impact on the overall behavior of the circulatory system. The analytically determined data in Table 2.4 suggest that the media is in compression in the axial and in tension in circumferential direction in the unloaded state of the abdominal aorta and has negative curvatures in both directions in the (nearly) stress-free reference state. Negative curvatures are modeled by sections of the outer surface of a torus. Similar to the intima, a closed mathematical description of the subarea having both constant width and length on the torus surface is not possible, thus, (2.28) needs to be modified again that the axial length of the media strip is constant over the entire circumferential dimension. Therefore, the parameter transformation of $\phi = \phi(\bar{\phi}, \theta)$ is repeated using the scaling factor

$$f^{(\mathrm{M})}(\theta) = \frac{R + r\cos\theta}{R + r}, \tag{2.31}$$

where $f^{(\mathrm{M})}(\theta) \leq 1$. This factor transforms the rotation angle according to $\phi(\bar{\phi}, \theta) = \bar{\phi}/f^{(\mathrm{M})}(\theta)$ and hence (2.28) can be rewritten as

$$\mathbf{X}^{(\mathrm{M})}(\theta, \phi) = \begin{bmatrix} (R + r\cos\theta)\sin(\bar{\phi}/f^{(\mathrm{M})}(\theta)) \\ r\sin\theta \\ (R + r\cos\theta)\cos(\bar{\phi}/f^{(\mathrm{M})}(\theta)) \end{bmatrix}. \tag{2.32}$$

This parametric equation defines a surface used to approximate the media in the (nearly) stress-free configuration. Superposition of seven surfaces leads to the definition of six individual layers of linear hexahedral elements through the thickness. The (nearly) stress-free reference configuration of the media is shown in Fig. 2.6 denoted by $\Omega_0^{(\mathrm{M})}$.
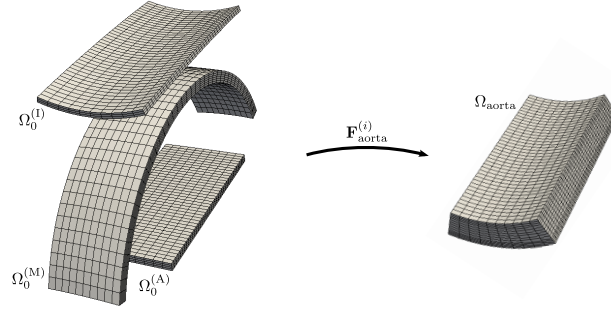
Figure 2.6: Numerical reconstruction of a model of an abdominal aorta (longitudinal segment) from the individual (nearly) stress-free reference configuration of intima, media, and adventitia ($\Omega_0^{(\mathrm{I})}$, $\Omega_0^{(\mathrm{M})}$, and $\Omega_0^{(\mathrm{A})}$, respectively) to the unloaded state. A necessary intermediate state to combine the arterial layers is not indicated, however, needed to merge the three layers and form the tissue composite.

Reference Geometry of the Adventitia. The adventitia in the validation example is, according to data provided in Table 2.4, in tension for both axial and circumferential direction in the unloaded *ex situ* configuration of the abdominal aorta. In addition, it is important to emphasize that it remains flat in axial direction after layer separation and only a small negative curvature in circumferential direction is observed. In contrast to the intima and the media, where modified versions of a torus surface are used to model the (nearly) stress-free reference configurations, the adventitia can be approximated without modification by the parametric equation of a right circular cylinder surface. Thus,

$$\mathbf{X}^{(\mathrm{A})}(\theta) = \begin{bmatrix} h \\ R\cos\theta \\ R\sin\theta \end{bmatrix}, \tag{2.33}$$

where superposition of five right circular cylinder surfaces represent four layers of linear hexahedral elements through the thickness. The (nearly) stress-free reference configuration of the adventitia is indicated in Fig. 2.6 denoted by $\Omega_0^{(\mathrm{A})}$.

Numerical Reconstruction of the Abdominal Aorta. In order to validate the assumptions made during analytic residual stretch/stress calculation as well as to verify the proposed FE framework for including residual stretches/stresses into patient-specific models of AAAs, the (nearly) stress-free reference configurations of the individual arterial layers $\Omega_0^{(i)}$ ($i \in [\mathrm{I, M, A}]$) are numerically reconstructed to form the unloaded *ex situ* state of an abdominal aorta Ω_{aorta} (see Fig. 2.6). Necessary kinematic transformations are described by the deformation gradients $\mathbf{F}_{\mathrm{aorta}}^{(i)}$ ($i \in [\mathrm{I, M, A}]$). A total number of 5200 elements are used to represent the reference geometry in appropriate detail, where 13 elements (3, 6,

and 4 for the intima, media, and adventitia, respectively) are used through the thickness to adequately model the bending dominant FE analysis. In order to compare the numerical results to the analytical solution obtained in [25], the same constitutive equations (a neo-Hookean material) with material parameters taken from Table 2.3 are used. The conforming unloaded state of the abdominal aorta Ω_{aorta} is achieved by a split of the overall deformation into two separate domains, not indicated in Fig. 2.6. Initially, the stress-free reference configurations of the three layers are transformed into cuboids, where combination (merging process) is performed. Subsequent deformation into the unloaded state Ω_{aorta} completes the numerical tissue reconstruction process.

3 SIMULATIONS AND ANALYTICAL RESULTS

3.1 Finite Element Mesh Quality Inspection

Mesh quality measures such as the scaled Jacobian should detect inverted (invalid) elements in the FE mesh in order to avoid the loss of fidelity or even cause a halt of the simulation prematurely. In addition, they should provide an estimate about the expected accuracy of the calculation, i.e., that requirements concerning the size of error are satisfied. The scaled Jacobian mesh quality metric defined in (2.1) and (2.2) can only be applied to regular hexahedral elements having eight vertices at different spatial locations in three-dimensional space. Therefore, collapsed hexahedral elements (e.g., wedge-shaped or pyramid-shaped elements) are identified and excluded from the mesh quality analysis. The number of collapsed elements and the degree of collapse for the AAA wall and the ILT are given for a representative example in Table 3.1. The obtained results indicate that

	$\#_{nodes}$	$\#_{nodes}$-1	$\#_{nodes}$-2	$\#_{nodes}$-3
AAA	19440	-	-	-
ILT	3966	252	324	276

Table 3.1: Number of hexahedral elements with their degree of collapse in the AAA wall and the ILT for the representative example. In general, (linear) hexahedrons are constituted by eight nodes at different spatial locations ($\#_{nodes} = 8$).

degenerated hexahedral elements are not present in the AAA wall due to the sophisticated meshing algorithm used. However, a total number of 852 elements with different degrees of collapse are found in the ILT (indicated by the black region at the boarder of the ILT in Fig. 3.1(c)), a necessity since the ILT is not present throughout the whole AAA.

Application of the proposed quality metric to the used FE mesh and analyzation of results obtained for the AAA wall given in Figs. 3.1(a) and (b) indicate that the initial element quality is generally at a very high level. All elements exhibit a scaled Jacobian above 0.2 and only for 4.75 % of the total number of hexahedral elements the value is less than 0.5. Results for the ILT, the AAA thrombus, in Figs. 3.1(c) and (d) indicate again high quality elements. Scaled Jacobians of 1.26 % of all elements in the ILT exhibit a value smaller than 0.5 and only for 0.05 % of the total number of elements values below 0.2 are observed. Again, it is important to emphasize that collapsed elements are excluded from this analysis since the quality metric is not applicable in this case. Detailed information concerning the
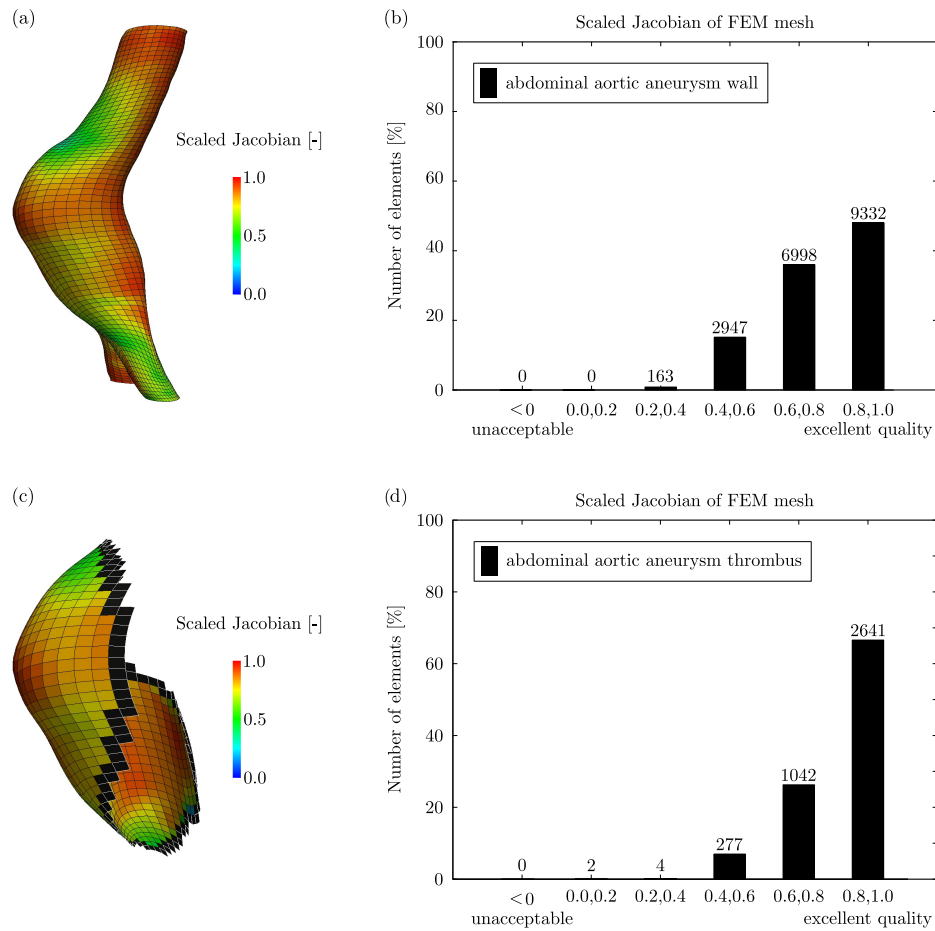
Figure 3.1: Global distribution of the scaled Jacobian quality measurement for (a) the AAA
wall and (c) the AAA thrombus, respectively. Histograms of mesh quality dis-
tribution, again for (b) the AAA wall and (d) the AAA thrombus, in order to
indicate high quality of the used FE mesh with the number of actual quality
counts on top of histogram bars. Black region (at the boarder of the ILT) in
(c) corresponds to collapsed elements, i.e., the region in which element quality
evaluation is not performed.

mesh quality in the individual layers of the AAA wall and the ILT for different quality
ranges is provided in Table 3.2.

The conforming hexahedral FE mesh used for analysis is a compromise between expected
computation time and simulation accuracy. The semi-automatic meshing algorithm devel-
oped is capable to generate meshes with higher density, nevertheless an increase in the
number of elements does not markedly change the quality distribution (cf., [62]). It is
assumed that a higher mesh density does not affect stress and deformation prediction sig-

Scaled Jacobian	<0	0.0,0.2	0.2,0.4	0.4,0.6	0.6,0.8	0.8,1.0
adventitia	-	-	89	1054	2302	3035
media	-	-	30	986	2316	3148
intima	-	-	44	907	2380	3149
abluminal	-	-	3	187	442	690
medial	-	-	-	71	339	912
luminal	-	2	1	19	261	1039

Table 3.2: Distribution of scaled Jacobian values for individual layers in the AAA wall and the AAA thrombus. Collapsed elements (284 degenerated hexahedral elements are present in every layer of the AAA thrombus) are not included in the analysis of the mesh quality inspection.

nificantly, where a mesh convergence study would be needed to support this assumption.

3.2 Validation of Residual Stretch/Stress

The methodology is validated by recreating analytically-determined three-dimensional residual stress distributions from [25] using data indicated in Table 2.4 via numerical reconstruction of a model of an abdominal aorta. In contrast to the method presented in [25] both axial and circumferential stretches and curvatures are approximated and a comparison is provided in Fig. 3.2. Figures 3.2(a), (c) and (e) indicate the three-dimensional stress components versus the normalized radius for the three-layer arterial tissue composite in the unloaded, residually stressed state for the circumferential, axial, and radial direction, respectively. Simulated results are generated from FE element stresses in corresponding directions located at the center of the model to minimize effects of boundary conditions. The corresponding three-dimensional FE representations of stresses are shown in Figs. 3.2(b), (d) and (f). Particularly, Fig. 3.2(c) shows an equilibrium stress distribution versus the normalized radius to ensure that the axial load at both ends of the aortic tissue model is zero, consistent with the definition in [25]. Therefore, the mean axial stress $\bar{\sigma}_{zz}$ is substracted from the stresses predicted in the FE simulation $\tilde{\sigma}_{zz}$, i.e., $\sigma_{zz} = \tilde{\sigma}_{zz} - \bar{\sigma}_{zz}$. Calculation of the mean axial stress $\bar{\sigma}_{zz}$ is performed in a slightly different manner compared to the analytical example in [25] because of the discrete nature and possible irregularities (numerical rounding issues) in the FE mesh after simulation. Thus,

$$\bar{\sigma}_{zz} = \frac{\sum_{i=1}^{n} \bar{\sigma}_{zz}^{i} A^{i}}{\sum_{i=1}^{n} A^{i}}, \tag{3.1}$$

where n is the number of elements located at the model center through the thickness of all individual layers chosen to be 13 (stated in Section 2.7). Evaluation of (3.1) leads to a
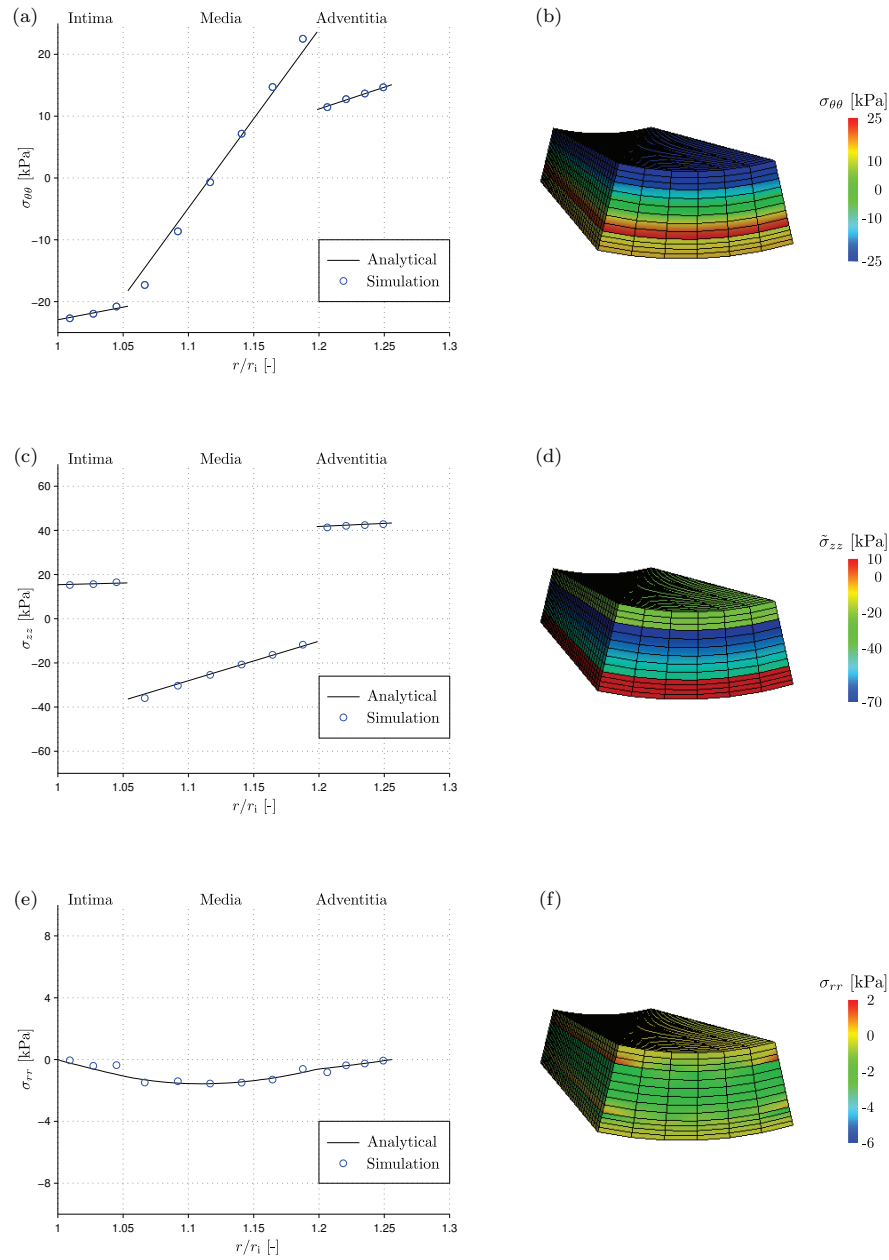
Figure 3.2: Three-dimensional stress components versus normalized radius for the three-layer arterial tissue model (intima, media, and adventitia) in the unloaded, residually stressed configuration ((a), (c), and (e)) and corresponding three-dimensional FE representations ((b), (d), and (f)): (a),(b) circumferential stress $\sigma_{\theta\theta}$; (c) modified axial stress for traction free ends σ_{zz} and (d) axial stress $\tilde{\sigma}_{zz}$; (e),(f) radial stress σ_{rr}.

mean axial stress of $\bar{\sigma}_{zz} = -32.80\,\text{kPa}$ in the FE model compared to $-33.27\,\text{kPa}$ stated in the analytical example of [25].

In general, the results obtained in this validation suggest that the assumption to neglect minor and only model major curvatures in the (nearly) stress-free reference configuration of the individual arterial tissue layers, as performed in [25], does not influence the residual stress distribution significantly (cf., the analytical and numerical determined stress contours in Figs. 3.2(c) and (e) for axial and radial stress, respectively). The circumferential stresses in the intima as well as the adventitia (see Fig. 3.2(a)) can also be captured with sufficient accuracy. However, in the media the FE simulations predicts a steeper gradient for the circumferential stress in radial direction than the analytical example in [25]. This finding can be explained by the additional curvature included in the FE analysis, which introduces additional bending stresses in the problem.

3.3 Residual Stretch/Stress Inclusion

Numerous crucial steps towards the consistent incorporation of residual stretches/stresses into patient-specific FE simulations of AAAs are performed, where information concerning the fundamental procedure has been provided in Section 2.6. Essential benchmarks with corresponding results obtained within the computational preprocessing phase are presented to illustrate the capabilities of the novel approach and the correctness of the implementation. In particular, plots for principal residual stretches obtained by numerical evaluation of analytic expressions (2.12)-(2.14) and frequency distributions for the 'normalized' distance, crucial in the proposed mapping procedure of residual stretches onto individual Gauss quadrature points, are presented.

3.3.1 Residual Stretch/Stress Modification

Verification of the geometrical assumptions made in [25] are essential for further analysis and form the basis for the proposed methodology to include residual stretches/stresses into patient-specific FE simulations of AAAs. Relations (2.12)-(2.14) characterize analytically the kinematic transformations performed in the validation for $c^{(\text{M})^2} = c^{(\text{M})} = 1$, where the principal stretch distribution for the three-layer arterial tissue complex is shown in Fig. 3.3(a). Reasonable principal stretch values are obtained in the intima as well as the adventitia. However, the principal stretches in the media tend to be extremely high and are therefore not considered as physiologically relevant, e.g., at the center of the media principal stretches of 1.454, 1.404, and 0.49 are obtained for circumferential, radial, and axial direction, respectively. A necessary minor adjustment factor $c^{(\text{M})}$ is introduced in a way it is not inverting the overall or affecting the tendency of the principal stretch distribution in the media. In addition, the incompressibility constraint presented in (2.15) needs to be fulfilled, leading to (2.12)-(2.14) with $c^{(\text{M})^2} = 1.5$ (media stretch-modification parameter). Figure 3.3(b) shows the principal stretch distributions including the media stretch-modification parameter, leading to more physiological residual stretch values of 1.187,
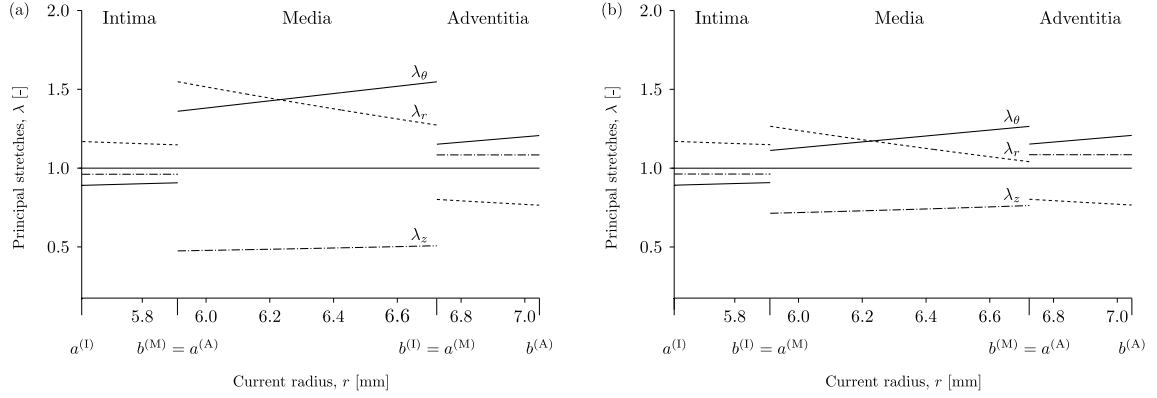
Figure 3.3: Residual stretch distributions versus radial coordinate through the intima, media, and adventitia of the arterial wall model. The solid, dashed, and dashed-dotted curves correspond to principal stretches in circumferential λ_θ, axial λ_z, and radial direction λ_r, respectively. Principal residual stretches are calculated using data from Table 2.3: (a) reproduced results of [25]; (b) modified principal residual stretch distribution to obtain physiological residual stretch values.

1.146, and 0.735 for circumferential, radial, and axial direction, respectively (measured at the center of the media). Subsequent results are obtained using the modified principal stretch values obtained via (2.12)-(2.14) with $c^{(\mathrm{M})^2} = 1.5$ and indicated in Fig. 3.3(b).

3.3.2 Identification of Gauss Point Location

An important step towards the correct inclusion of residual stretches into patient-specific FE models of AAAs is the pragmatic mapping procedure described in Section 2.6.2. An essential quantity within this process is the 'normalized' distance $f_j^{(i)}$ calculated for every Gauss quadrature point j in every arterial tissue layer i, where $i \in [\mathrm{I}, \mathrm{M}, \mathrm{A}]$. This numeric/geometric measure determines the amount of residual stretch included at a certain Gauss integration point within the FE mesh via (2.20), where it is important to note that $f_j^{(i)} \in [0, 1]$. Figure 3.4 shows determined values for the 'normalized' distance in the three arterial layers with corresponding histograms, providing information about the frequency distribution of specific values. Numerical integration in FE simulations is conveniently performed by Gauss quadrature, the most accurate quadrature formula for polynomial expressions [73]. Multi-dimensional integration in so-called natural coordinates, e.g., integration over a three-dimensional domain with coordinates ξ, η, and ζ in the range of $-1 < \xi, \eta, \zeta < 1$, is performed by

$$\int_{-1}^{1}\int_{-1}^{1}\int_{-1}^{1} f(\xi, \eta, \zeta)\,\mathrm{d}\xi\,\mathrm{d}\eta\,\mathrm{d}\zeta = \sum_{j=1}^{n}\sum_{k=1}^{n}\sum_{l=1}^{n} f(\xi_j, \eta_k, \zeta_l)w_j w_k w_l, \qquad (3.2)$$
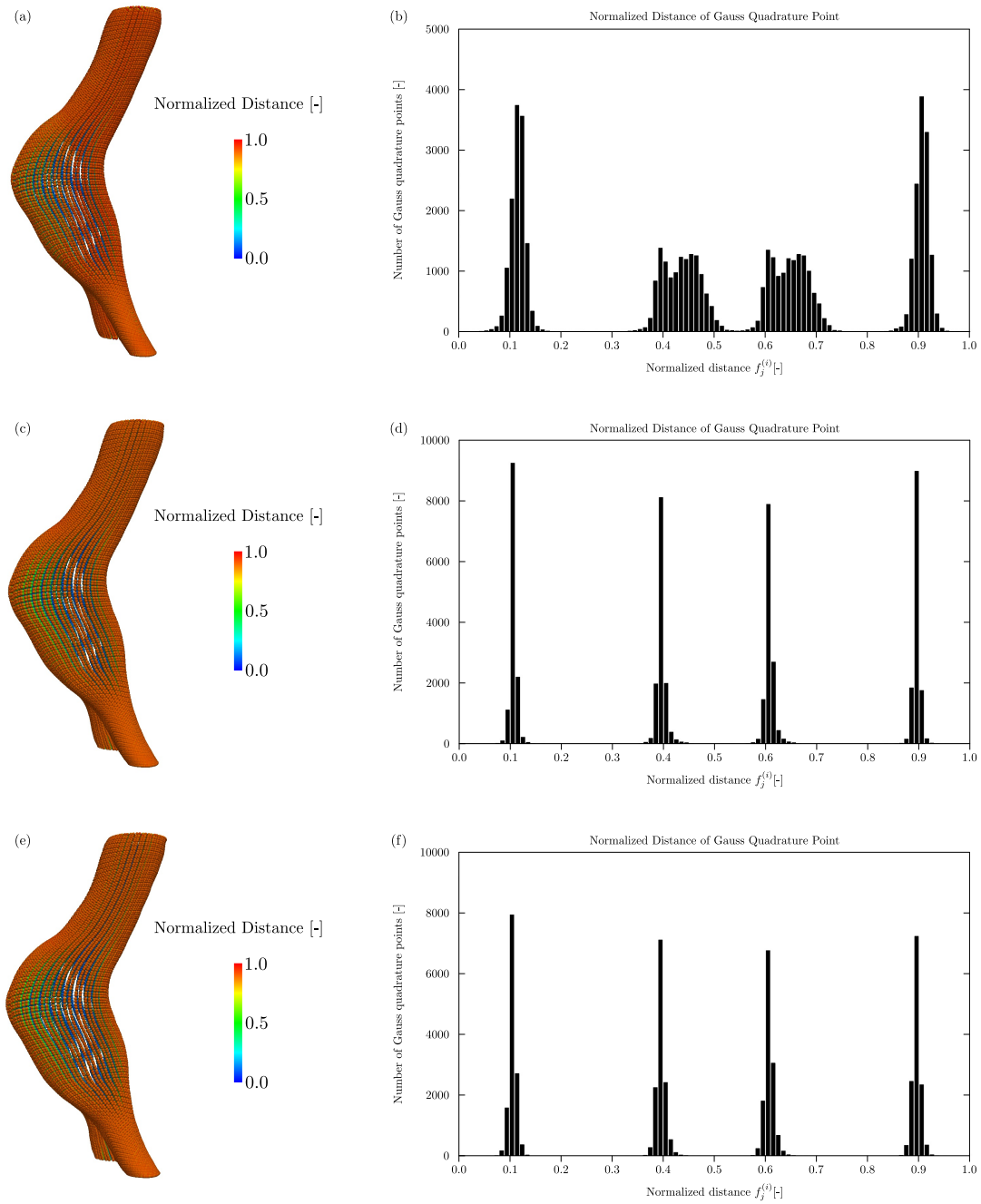
Figure 3.4: 'Normalized' distance values $f_j^{(i)}$ ((a), (c), and (e)) for every individual Gauss quadrature point in the FE mesh of the AAA wall and corresponding histograms, indicating the frequency distribution ((b), (d), and (f)) for the intima, media, and adventitia, respectively.

where ξ_j, η_k, and ζ_l are the points at which the function is evaluated using corresponding weights w_j, w_k, and w_l. Thus, the Gauss quadrature with an n-point formula is capable to integrate a polynomial of order $2n - 1$ exact. The location of Gauss quadrature points in three-dimensional linear (i.e., elements with linear interpolation function) hexahedral elements in natural coordinate direction ξ is given by $\xi_{1,2} = \pm 1/\sqrt{3}$, having weights of $w_{1,2} = 1$. Hence, the 'normalized' distances $f_j^{(i)}$ in direction of $\bar{\mathbf{n}}_j^{(i)}$ for two perfectly aligned ideal elements, i.e., cubes, having a total edge length of 1 correspond to the location of the Gauss quadrature points within these elements. Explicit values for these 'normalized' distances are determined to be $(1 \pm 1/\sqrt{3})/4$ and $(3 \pm 1/\sqrt{3})/4$, consistent with regions of the largest frequency distribution magnitude found in Figs. 3.4(b), (d), and (f).

The overall distribution of 'normalized' distance values is shown in Figs. 3.4(a), (c), and (e) for the intima, media, and adventitia, respectively. The corresponding frequency distributions indicate that the proposed method is able to calculate these values in an adequate manner. Excellent distributions for the media and the adventitia (see Figs. 3.4(d) and (f)) are obtained having maximum/minimum 'normalized' distance values of $0.939/0.017$ and $0.955/0.033$, respectively. Calculated values in the intima, which is significantly thinner compared to the media and adventitia, indicate that the method still leads to an acceptable result. However, the distribution of individual values is more diverse with a maximum/minimum of $1.000/0.000$. This result suggests that the error introduced into the proposed method by fitting the planes ${}^{\text{i}}\Gamma_j^{(i)}$ and ${}^{\text{o}}\Gamma_j^{(i)}$ via orthogonal distance regression becomes larger with decreasing layer thickness, consistent with expectations.

3.4 Stresses in Abdominal Aortic Aneurysm

Results obtained using the novel methodology to include residual stretches/stresses into patient-specific FE simulations of a AAA are provided in the following. The patient considered suffering from a AAA is assumed to have a DBP of 85 mmHg and a SBP of 135 mmHg, classified as 'Prehypertension' according to [7]. It is assumed that medical imaging, i.e., MRI, is performed at DBP, important for pressurization using the proposed GPA [68].

3.4.1 Comparison of Diastolic Stress Distributions

In order to investigate the effect of initial stresses, which includes both residual stresses and prestresses, on the stress distribution within the ILT and the AAA wall different simulations are performed: (i) a conventional computation neglecting both residual stresses and prestresses in the following termed 'historical' calculation, (ii) a computation accounting only for prestresses using the GPA proposed in [68] termed 'prestressing' calculation, and (iii) a computation including the three-dimensional nature of residual stresses as well as prestresses by performing the proposed algorithm termed as 'novel' calculation. Figure 3.5 shows circumferential stress distributions $\sigma_{\theta\theta}$ for all three types of computational models at an internal pressure (DBP) of 85 mmHg. Figures 3.5(a)-(c) correspond to results for the
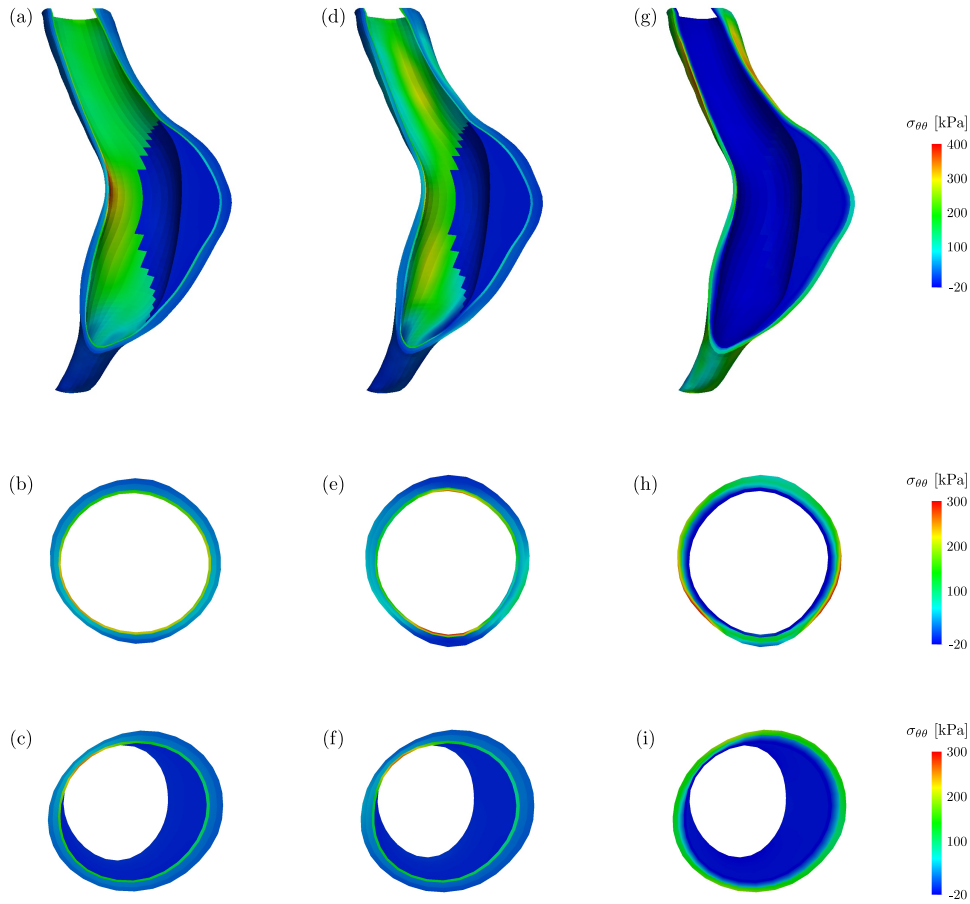
Figure 3.5: Circumferential stress $\sigma_{\theta\theta}$ in the ILT and the AAA wall at a DBP of 85 mmHg for the three different types of simulations performed: (a),(b), and (c) 'historical' calculation; (d),(e), and (f) 'prestressing' calculation and (g),(h), and (i) 'novel' calculation. 'Healthy' arterial tissue is assumed in the upper part of the AAA where an ILT is absent ((b), (e), and (h)), while the 'diseased' aorta is located in the center region of the AAA ((c), (f), and (i)).

'historical' calculation, Figs. 3.5(d)-(f) indicate stress distributions using the 'prestressing' calculation and Figs. 3.5(g)-(i) provide results obtained using the 'novel' approach. Slices indicating the different stress distributions at two vertical positions are provided to evaluate the difference between the algorithms for 'healthy' (the ILT-free upper part of the AAA is assumed to represent healthy arterial tissue, see Figs. 3.5(b), (e), and (h)) and 'diseased' abdominal aortic tissue (region in the AAA covered by an ILT is assumed to be diseased, see Figs. 3.5(c), (f), and (i)).

3.4.2 Comparison of Systolic Stress Distributions

Calculations performed for DBP represent the distinct level of pressurization of the AAA at which medical imaging, i.e., MRI, was performed. Thus, up to that particular phase of the analysis the used algorithms differ as described earlier to account for various loading situations. Due to material non-linearity the results of any subsequent simulation will differ remarkably, even if the algorithm used is identical for all three cases. The nomenclature introduced in Section 3.4.1 is kept to distinguish between performed calculations. The patient considered in this analysis is assumed to have a SBP of 135 mmHg, which
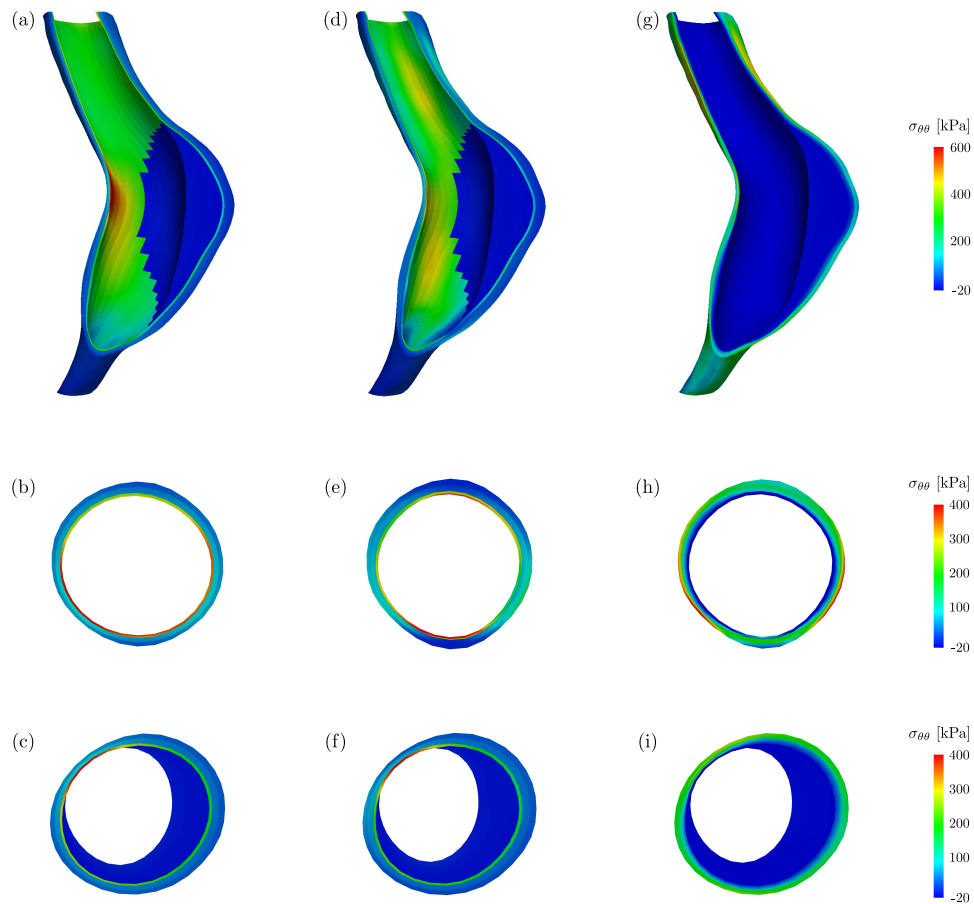
Figure 3.6: Circumferential stress $\sigma_{\theta\theta}$ in the ILT and the AAA wall at a SBP of 135 mmHg for the three different types of simulations performed: (a),(b), and (c) 'historical' calculation; (d),(e), and (f) 'prestressing' calculation and (g),(h), and (i) 'novel' calculation. 'Healthy' arterial tissue is assumed in the upper part of the AAA where an ILT is absent ((b), (e), and (h)), while the 'diseased' aorta is located in the center region of the AAA ((c), (f), and (i)).

also corresponds to a slightly elevated value compared to normal conditions. Figure 3.6 shows circumferential stress distributions $\sigma_{\theta\theta}$ for all three types of computational models at an internal pressure (SBP) of 135 mmHg. Figures 3.6(a)-(c) correspond to results for the 'historical' calculation, Figs. 3.6(d)-(f) indicate stress distributions using the 'prestressing' calculation and Figs. 3.6(g)-(i) provide results obtained using the 'novel' approach. For consistency reasons, again stress results are evaluated at two vertical positions (same location as in Fig. 3.5) representing 'healthy' (see Figs. 3.6(b), (e), and (h)) and 'diseased' (see Figs. 3.6(c), (f), and (i)) aortic tissue on top of the overall stress distributions within the ILT and the AAA wall for all different calculations (see Figs. 3.6(a), (d), and (g)).

3.5 Displacement Magnitude Evaluation

As a consequence of the distinct implementation of the three algorithms compared, i.e., 'historical', 'prestressing', and 'novel' computation, individual displacement fields are obtained. The magnitude of nodal displacements $\|\mathbf{u}\|$ provides another important quantity in the comparison of the three algorithms and is indicated in Fig. 3.7 for DBP. The maximum nodal displacement magnitude obtained using the 'historical' calculation (see Fig. 3.7(a)) is 3.24 mm. Since both the 'prestressing' calculation as well as the 'novel' calculation are programmed to maintain the imaged *in vivo* configuration after pressurization to DBP, no displacement is observed (see Figs. 3.7(b) and (c)), indicating correctness of the implementation of these methods.
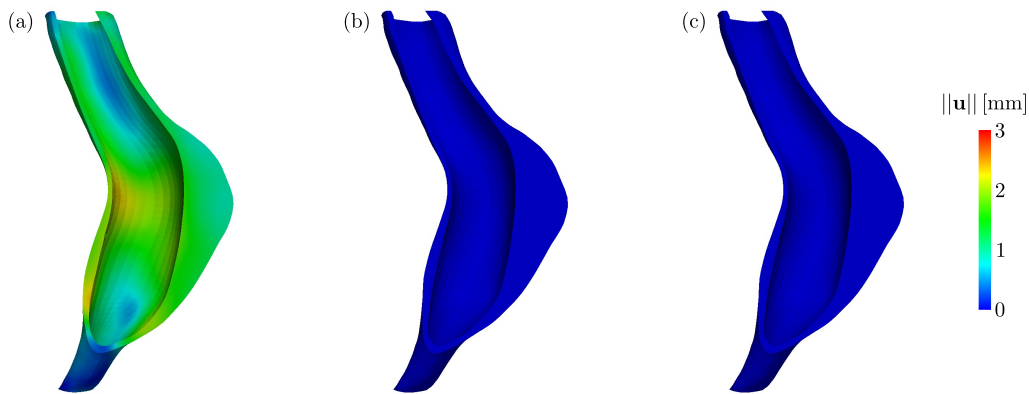
Figure 3.7: Distribution of nodal displacement magnitudes $\|\mathbf{u}\|$ obtained at DBP using the three different algorithms: (a) 'historical' calculation, (b) 'prestressing' calculation, and (c) proposed 'novel' algorithm including residual stresses and prestresses.

A subsequent pressure increase to SBP leads to a maximum nodal displacement magnitude $\|\mathbf{u}\|$ of 3.61 mm in the 'historical' calculation (see Fig. 3.8(a)). Significantly differ-
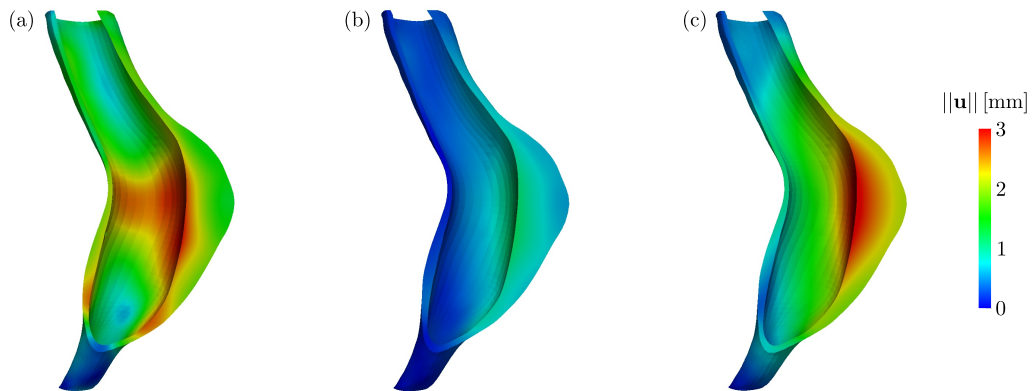
Figure 3.8: Distribution of nodal displacement magnitudes $\|\mathbf{u}\|$ obtained at SBP using the three different algorithms: (a) 'historical' calculation, (b) 'prestressing' calculation, and (c) proposed 'novel' algorithm including residual stresses and prestresses.

ent distributions are obtained for the 'prestressing' (see Fig. 3.8(b)) and the 'novel' (see Fig. 3.8(c)) algorithm, being notably larger in the latter one. The maximum nodal displacement magnitudes $\|\mathbf{u}\|$ for the 'prestressing' and the 'novel' calculation are determined to be 1.18 mm and 3.13 mm, respectively.

4 DISCUSSION AND CONCLUDING REMARKS

4.1 Discussion on Results in Abdominal Aortic Aneurysms

Obtained stress and displacement distributions for the three individual computations performed at DBP and SBP are discussed in the following. Mechanical modeling of complex three-dimensional biological structures such as AAAs includes several assumptions and limitations influencing the outcome. Therefore, potential impacts on stress and displacement predictions are discussed.

4.1.1 Comparison of Stress Distributions

A quantitative comparison of circumferential stress distributions $\sigma_{\theta\theta}$ obtained using the three algorithms ('historical', 'prestressing', and 'novel' calculation) at DBP provided in Figs. 3.5(a), (d), and (g) suggests that the predicted mean stress magnitude in the intima using the 'historical' and the 'prestressing' calculation are non-physiological and unrealistically high. This is in contrast to observed mean stresses in the media and adventitia, where stress estimates seem to be very small and basically non-existing. The 'novel' algorithm to include residual stresses in patient-specific FE simulations of arterial tissue provides reasonable mean stress magnitudes in circumferential direction for the media and adventitia. However, stress estimates in the intima may be too small (compressive mean circumferential stress is observed). Notable differences in stress distributions are found for 'healthy' and 'diseased' arterial tissue using the 'novel' approach, where stress peaks in the adventitia vanish in the latter (cf., Figs. 3.5(h) and (i)).

A dramatic increase in mean circumferential stress values is obtained in the intima for the 'historical' and the 'prestressing' calculation due to exponential stiffening of the collagen fiber fabric in the high load regime (see Figs. 3.6(a)-(f)). However, only minor stress increase is observed in the media and adventitia as a consequence of the geometrical non-linearity of the problem. It is assumed that the intima stress-shields the media and adventitia, leading to this moderate increase in stress values at SBP. The 'novel' algorithm predicts more reasonable mean stress values in the media and adventitia. Slightly increased, but still negative circumferential stresses are observed in the intima (see Figs. 3.6(g)-(i)). Again, notable differences between 'healthy' and 'diseased' arterial tissue can be identified (cf., Figs. 3.6(h) and (i)), where the circumferential stress distribution $\sigma_{\theta\theta}$ seems to be more uniform in the 'novel' simulation compared to the 'historical' and the 'prestressing' calculation.

The 'novel' approach, in which prestresses and residual stresses are included, leads to physiologically relevant mean stress values for the media and adventitia at DBP and SBP, however, a small compressive stress in circumferential direction is observed in the intima. The reason for this non-physiological stress estimate might be an overprediction of residual stretches in the analytical calculation performed prior to FE simulation (discussed in detail in Section 4.2.2). Therefore, a parameter study of the influence of the residual stretches on variations in mean circumferential stress $\sigma_{\theta\theta}$ is performed, leading to expected positive mean stress values in the intima at DBP if adequately chosen. In addition, large variations in circumferential stress values $\sigma_{\theta\theta}$ are observed using the 'prestressing' and the 'novel' approach at both pressures (DBP and SBP), similar to findings in the literature [8, 59, 70]. A statistical significance between the local wall curvature and the predicted circumferential stress for the thoracic aorta was specified in [70], indicating that peak stresses are associated with large local curvatures (small local radii). Remarkable differences in lumen shape are observed when the 'historical' calculation is compared to the 'prestressing' and the 'novel' approach (see Figs. 3.5(b), (e), and (h) for DBP and Figs. 3.6(b), (e), and (h) for SBP). Smooth curvatures are obtained in the 'historical' simulations, in contrast to the 'prestressing' and the 'novel' (geometry conserving algorithms) calculation, where large curvature differences are still present and possibly explaining the large stress variations. Thus, there is a need for experimental investigations to determine variations in local material parameters [32] and residual stress data [40], which will likely homogenize the overall stress state.

The stress results obtained in the ILT for all simulations performed indicate a state of hydrostatic compression. However, due to the lack of experimental data the mechanical behavior of the individual ILT layers under compression remains unknown. Thus, the constitutive model used may not be an adequate representation of the tissue composite in compression and stress results should be treated with caution.

In general, the 'novel' approach has the potential to increase the reliability of stress predictions within AAA walls since the overall mean stresses of the individual arterial layers become substantially more homogeneous at higher loads such as SBP. In addition, compressive circumferential stresses (hoop stresses) at the inner boundary of the arterial wall using prestressing algorithms in combination with residual stresses are reported in the literature, e.g., [1, 2, 70].

4.1.2 Comparison of Displacement Distributions

The influence of residual stretches/stresses is not only noticeable in the stress pattern as discussed earlier, but also the overall deformation field changes significantly for the three different simulations performed as depicted in Figs. 3.7 and 3.8. Large nodal displacement magnitudes for the 'historical' calculation are predicted at DBP and only a small increase is observed at SBP. This fact can be explained by exponential stiffening of the collagen fiber fabric in the AAA wall, only enabling large displacements in the low load regime. No

displacement is observed for the 'prestressing' and the 'novel' calculation at DBP, indicating correctness of the implemented GPA (the imaged *in vivo* geometry is maintained). However, a large difference in nodal displacement magnitudes for both algorithms is obtained in the systolic phase of the cardiac cycle. While diastolic circumferential stresses in the intima for the 'prestressing' calculation are already high, suggesting that a pronounced stiffness is present, they are more moderate in the layers for the 'novel' calculation. For this reason, additional pressure increase has a larger impact on nodal displacement magnitudes. Nodal displacements for all individual algorithms investigated are largest in the 'historical' calculation, consistent with findings in [1].

Obtained results indicate that larger nodal displacement magnitudes in the AAA wall covered by the ILT are predicted by the 'novel' calculation compared to the 'historical' one (see Figs. 3.8(a) and (c)). A possible explanation for this effect might be the distinct kink of the overall AAA geometry in combination with axial residual stresses.

4.2 Limitations of Novel Approaches

The proposed method to include residual stresses in patient-specific FE models of arterial tissue is applied to a AAA within this thesis. In general, this approach is applicable to any residually stressed material where specific data on residual deformations are available. It is intended to provide a method more accurately predicting the overall stress state within biological structures. In the context of AAA simulations the accurate prediction of stress may lead to an increase in reliability of rupture potential characterization. Novel challenges arise from more sophisticated modeling approaches and thus assumptions and limitations are discussed in detail to highlight the additional complexity.

4.2.1 Residual Stretch/Stress Validation

In the analysis performed to validate the novel approach of including residual stresses into patient-specific FE simulations it is assumed that the reference configuration of the separated layers is totally stress-free. However, in [40] it was suggested that additional cuts through the arterial tissue may be necessary to obtain a zero-stress state. In theory the arterial wall would need to be separated into infinitesimally small parts to finally obtain a state without any stresses present [34, 49]. Determination of curvatures in axial and circumferential direction in [26] was performed by approximating the actual geometry by circular arcs. The influence of this circularity assumption was investigated in [50] and is confirmed to be a reasonable approximation.

The (nearly) stress-free reference configuration of the adventitia remains fairly simple and thus stretches and curvatures in both directions can be represented by subsections of right circular cylinder surfaces. Nevertheless, it is more complex for the intima and the media, where modeling introduces several approximations. Sliding surfaces and torus surfaces provide feasible geometries to represent these reference configurations. Individual parameterizations using sliding surfaces would be necessary for intima and adventitia, in contrast

to the torus surface capable to model both reference configurations. The representation of curvatures and stretches in the reference configuration might be more accurate towards the edges of the individual layers using sliding surfaces, however, element distortion could be more pronounced. The main focus of this validation is to identify the influence of the approximation made by neglecting the minor curvature in the stress-free configuration. Since both geometries are able to model all quantities at their center perfectly, decision is made for the torus surface and no specific error analysis on the feasible geometries is performed. The torus surface parameterization is modified in order that the axial length of the strips is constant over the entire circumferential direction since axial dimensions are the predominant ones in the validation analysis. This introduces an increasing error (not further quantified) in circumferential dimensions towards the axial edges. The circumferential curvatures of the intima and the media are assumed to be more important in the present analysis and thus, modeling of these curvatures is performed accurately. This assumption introduces an increasing error in axial curvature towards the circumferential boundaries of the tissue strips. However, it should be emphasized that stretches as well as curvatures are accurately modeled in both directions at the origin of the coordinate system used. Because of this reason, stress analysis subsequent to numerical tissue reconstruction is only performed at the elements connected to the center of the unloaded configuration Ω_{aorta}. This leads to a minimization of the error introduced by the approximations on the numerical reconstruction result and is assumed to be acceptable.

4.2.2 Simulations of Abdominal Aortic Aneurysm

The FE analysis performed in this thesis treats the AAA as a healthy abdominal aorta, assuming that the layered structure and the perfect collagen fiber alignment of the tissue are still present. However, research using second harmonic generation (SHG) imaging has identified that the diseased AAA wall covered by an ILT is fundamentally different in terms of macroscopic structure and fiber alignment to a healthy human abdominal aorta (cf., Figs. 4.1(a), (b), and (c)). In addition, biaxial mechanical tests of AAA walls confirmed a change in material properties compared to healthy abdominal aortas [63, 65]. Lipid pools and calcifications might be present in a AAA as indicated in Figs. 4.1(b) and (c) by the dense light green region and the small black holes, respectively. These structural components are not segmented during image processing and therefore not considered in FE simulations (analyses including lipid pools and/or calcifications have been performed in [28, 33]).

Due to the lack of residual stress data for diseased arterial tissue it remains unknown to what extent ILT formation and presence change residual wall stresses. It is assumed that this influence is negligible and residual stress data for healthy abdominal aortas are used. According to observations made in the laboratory of the Institute of Biomechanics at Graz University of Technology, residual stresses in the individual ILT layers are small and therefore not included in the FE analysis. Analytically determined residual stretches calculated in the preprocessing stage of the proposed method (cf., [25]) are based on modeling the
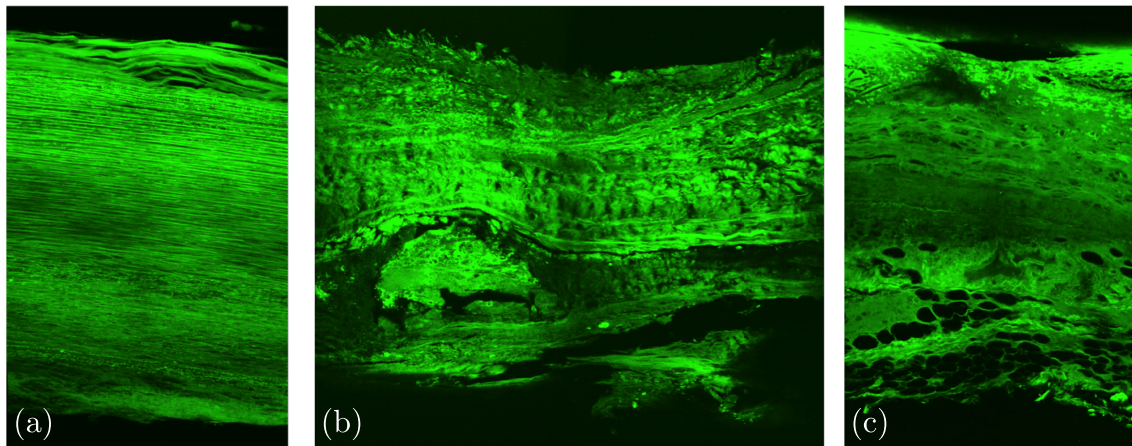
Figure 4.1: SHG cross-section images of (a) a human non-atherosclerotic abdominal aorta indicating nearly perfect fiber alignment; (b) and (c) a human AAA wall covered by an ILT where calcifications and lipid pools are observed. Pictures taken by H Wolinski, PhD with permission of AJ Schriefl, PhD (unpublished).

aortic tissue as a neo-Hookean material for convenience of the analysis. Residual stretches are likely small and the influence of exponential stiffening of collagen fibers is neglected. Thus, the calculated residual deformations could be overestimated, justifying the assumption to introduce a media stretch-modification parameter. However, due to this adjustment factor traction continuity at the intima-media and the media-adventitia interface may be lost. Performing a residual stress experiment includes the excision, i.e., unloading, of the artery from the human cadaver and subsequently cutting of axial and circumferential tissue strips. As a consequence, residual stresses are released, leading to an equilibrium configuration after some time of relaxation. This process indicates that residual stresses should be included in an unloaded arterial state. In the proposed approach MRI imaging is performed at DBP remaining the unloaded configuration unknown. Hence, calculated residual stresses are included in a loaded state of the artery within the proposed method (previous to pressure application via the GPA). The impact of this particular assumption on the predicted stress state cannot be quantified using the data available.

4.3 Concluding Remarks and Outlook

The novel approach to include residual stresses in patient-specific FE models of arteries and the corresponding results presented in this thesis should serve as a basis for further research in computational mechanics. The method developed is applied to a representative AAA, where many more patient-specific simulations need to be performed to demonstrate its general applicability. In order to fully characterize the stress state at a certain location within a living tissue, more sophisticated modeling approaches are required. This suggests

an additional need to account for active components such as smooth muscle contraction in FE simulations in addition to the passive behavior modeled. Fluid-structure interaction between the blood flow and the arterial wall can further improve prediction of *in vivo* stresses, however, introducing another level of complexity into existing FE simulations [43]. Novel challenges arise from using more complex algorithms, indicating the need for intensive research in the field of cardiovascular biomechanics. Sophisticated physical modeling imposes additional demands on improved experiments and measurements to better quantify patient-specific tissue parameters, e.g., regional material and residual stress parameters.

In the context of growth and remodeling the 'homogeneous stress hypothesis' is of fundamental importance (e.g., [47]). To this end, residual stresses must be considered since they generally lead to a more uniform stress field. Ultimately, it is the mechanical environment of individual cells, which is the driving force for processes associated with growth and remodeling. Hence, investigation in mechanobiology to better understand mechanotransduction (a molecular mechanism of a cell responding to mechanical stimuli) is likely a key to understand physiological adaption as well as the evolution of specific diseases.

REFERENCES

[1] V Alastrué, A García, E Peña, JF Rodríguez, MA Martínez, and M Doblaré. Numerical framework for patient-specific computational modelling of vascular tissue. *International Journal for Numerical Methods in Biomedical Engineering*, 26(1):35–51, 2010.

[2] V Alastrué, MA Martínez, and M Doblaré. Modelling adaptative volumetric finite growth in patient-specific residually stressed arteries. *Journal of Biomechanics*, 41(8):1773–1781, 2008.

[3] V Alastrué, E Peña, MA Martínez, and M Doblaré. Assessing the use of the 'opening angle method' to enforce residual stresses in patient-specific arteries. *Annals of Biomedical Engineering*, 35(10):1821–1837, 2007.

[4] L Antiga, B Ene-Iordache, L Caverni, GP Cornalba, and A Remuzzi. Geometric reconstruction for computational mesh generation of arterial bifurcations from CT angiography. *Computerized Medical Imaging and Graphics*, 26(4):227–235, 2002.

[5] L Antiga and DA Steinman. Robust and objective decomposition and mapping of bifurcating vessels. *IEEE Transactions on Medical Imaging*, 23(6):704–713, 2004.

[6] DH Bergel. *The Visco-Elastic Properties of the Arterial Wall*. Phd, University of London, United Kingdom, 1960.

[7] AV Chobanian, GL Bakris, HR Black, WC Cushman, LA Green, JL Izzo, Jr, DW Jones, BJ Materson, S Oparil, JT Wright, Jr, EJ Roccella, and the National High Blood Pressure Education Program Coordinating Committee. The seventh report of the Joint National Committee on prevention, detecion, evaluation, and treatment of high blood pressure: The JNC7 report. *Journal of the American Medical Association*, 289(19):2560–2571, 2003.

[8] S de Putter, BJBM Wolters, MCM Rutten, M Breeuwer, FA Gerritsen, and FN van de Vosse. Patient-specific initial wall stress in abdominal aortic aneurysms with a backward incremental method. *Journal of Biomechanics*, 40(5):1081–1090, 2007.

[9] G De Santis, M De Beule, K Van Canneyt, P Segers, P Verdonck, and B Verhegghe. Full-hexahedral structured meshing for image-based computational vascular modeling. *Medical Engineering & Physics*, 33(10):1318–1325, 2011.

[10] H Demiray. A note on the elasticity of soft biological tissues. *Journal of Biomechanics*, 5(3):309–311, 1972.

[11] TSE Eriksson. *Cardiovascular Mechanics: The Biomechanics of Arteries and the Human Heart.* Phd, Graz University of Technology, Austria, 2012.

[12] J Ferruzzi, DA Vorp, and JD Humphrey. On constitutive descriptors of the biaxial mechanical behaviour of human abdominal aorta and aneurysms. *Journal of the Royal Society Interface*, 8(56):435–450, 2011.

[13] DA Field. Qualitative measures for initial meshes. *International Journal for Numerical Methods in Engineering*, 47(4):887–906, 2000.

[14] C Fleming, EP Whitlock, TL Beil, and FA Lederle. Screening for abdominal aortic aneurysm: A best-evidence systematic review for the U.S. Preventive Services Task Force. *Annals of Internal Medicine*, 142(3):203–211, 2005.

[15] YC Fung. On the foundations of biomechancis. *Journal of Applied Mechanics*, 50(4b):1003–1009, 1983.

[16] TC Gasser, M Auer, F Labruto, J Swedenborg, and J Roy. Biomechanical rupture risk assessment of abdominal aortic aneurysms: Model complexity versus predictability of finite element simulations. *European Journal of Vascular and Endovascular Surgery*, 40(2):176–185, 2010.

[17] TC Gasser, RW Ogden, and GA Holzapfel. Hyperelastic modelling of arterial layers with distributed collagen fibre orientations. *Journal of the Royal Society Interface*, 3(6):15–35, 2006.

[18] MW Gee, C Förster, and WA Wall. A computational strategy for prestressing patient-specific biomechanical problems under finite deformation. *International Journal for Numerical Methods in Biomedical Engineering*, 26(1):52–72, 2010.

[19] MW Gee, C Reeps, HH Eckstein, and WA Wall. Prestressing in finite deformation abdominal aortic aneurysm simulation. *Journal of Biomechanics*, 42(11):1732–1739, 2009.

[20] S Haulon, C Lions, EP McFadden, M Koussa, V Gaxotte, P Halna, and JP Beregi. Prospective evaluation of magnetic resonance imaging after endovascular treatment of infrarenal aortic aneurysms. *European Journal of Vascular and Endovascular Surgery*, 22(1):62–69, 2001.

[21] A Henderson Squillacote. *The ParaView Guide. A Parallel Visualization Application.* Kitware Inc., 2007.

[22] GA Holzapfel. *Nonlinear Solid Mechanics. A Continuum Approach for Engineering.* John Wiley & Sons, Chichester, 2000.

[23] GA Holzapfel. Determination of material models for arterial walls from uniaxial extension tests and histological structure. *Journal of Theoretical Biology*, 238(2):290–302, 2006.

[24] GA Holzapfel, TC Gasser, and RW Ogden. A new constitutive framework for arterial wall mechanics and a comparative study of material models. *Journal of Elasticity*, 61(1-3):1–48, 2000.

[25] GA Holzapfel and RW Ogden. Modelling the layer-specific three-dimensional residual stresses in arteries, with an application to the human aorta. *Journal of the Royal Society Interface*, 7(46):787–799, 2010.

[26] GA Holzapfel, G Sommer, M Auer, P Regitnig, and RW Ogden. Layer-specific 3D residual deformations of human aortas with non-atherosclerotic intimal thickening. *Annals of Biomedical Engineering*, 35(4):530–545, 2007.

[27] GA Holzapfel, G Sommer, TC Gasser, and P Regitnig. Determination of layer-specific mechanical properties of human coronary arteries with nonatherosclerotic intimal thickening and related constitutive modeling. *American Journal of Physiology - Heart and Circulatory Physiology*, 289(5):H2048–H2058, 2005.

[28] GA Holzapfel, M Stadler, and CAJ Schulze-Bauer. A layer-specific three-dimensional model for the simulation of balloon angioplasty using magnetic resonance imaging and mechanical testing. *Annals of Biomedical Engineering*, 30(6):753–767, 2002.

[29] JD Humphrey. *Cardiovascular Solid Mechanics. Cells, Tissues, and Organs.* Springer, New York, 2002.

[30] JD Humphrey and GA Holzapfel. Mechanics, mechanobiology, and modeling of human abdominal aorta and aneurysms. *Journal of Biomechanics*, 45(5):805–814, 2012.

[31] GS Kassab. Biomechanics of the cardiovascular system: The aorta as an illustratory example. *Journal of the Royal Society Interface*, 3(11):719–740, 2006.

[32] J Kim and S Baek. Circumferential variations of mechanical behavior of the porcine thoracic aorta during the inflation test. *Journal of Biomechanics*, 44(10):1941–1947, 2011.

[33] DE Kiousis, SF Rubinigg, M Auer, and GA Holzapfel. A methodology to analyze changes in lipid core and calcification onto fibrous cap vulnerability: The human atherosclerotic carotid bifurcation as an illustratory example. *Journal of Biomechanical Engineering*, 131(12):121002, 2009.

[34] A Klarbring, T Olsson, and J Stålhand. Theory of residual stresses with application to an arterial geometry. *Archives of Mechanics*, 59(4-5):341–364, 2007.

[35] PM Knupp. Achieving finite element mesh quality via optimization of the Jacobian matrix norm and associated quantities. Part II - A framework for volume mesh optimization and the condition number of the Jacobian matrix. *International Journal for Numerical Methods in Engineering*, 48(8):1165–1185, 2000.

[36] PM Knupp. Achieving fnite element mesh quality via optimization of the Jacobian matrix norm and associated quantities. Part I - A framework for surface mesh optimization. *International Journal for Numerical Methods in Engineering*, 48(3):401–420, 2000.

[37] PM Knupp. Algebraic mesh quality metrics for unstructured initial meshes. *Finite Elements in Analysis and Design*, 39(3):217–241, 2003.

[38] PM Knupp. Remarks on mesh quality. In *Proceedings of the 45th AIAA Aerospace Sciences Meeting and Exhibit*, pages 1–10, Reno, 2007.

[39] S Lee, N Piersol, F Loth, P Fischer, G Leaf, B Smith, R Yedevalli, A Yardimci, N Alperin, and L Schwartz. Automated mesh generation of an arterial bifurcation based upon *in vivo* MR images. In *Proceedings of the 22nd Annual EMBS International Conference*, pages 719–722, Chicago, 2000.

[40] SQ Liu and YC Fung. Zero-stress states of arteries. *Journal of Biomechanical Engineering*, 110(1):82–84, 1988.

[41] JD MacDougall, D Tuxen, DG Sale, JR Moroz, and JR Sutton. Arterial blood pressure response to heavy resistance exercise. *Journal of Applied Physiology*, 58(3):785–790, 1985.

[42] FL Moll, JT Powell, G Fraedrich, F Verzini, S Haulon, M Waltham, JA van Herwaarden, PJE Holt, JW van Keulen, B Rantner, FJV Schlösser, F Setacci, and J-B Ricco. Management of abdominal aortic aneurysms clinical practice guidelines of the European Society for Vascular Surgery. *European Journal of Vascular and Endovascular Surgery*, 41(Suppl 1):S1–S58, 2011.

[43] DS Molony, S Broderick, A Callanan, TM McGloughlin, and MT Walsh. Fluid-structure interaction in healthy, diseased and endovascularly treated abdominal aortic aneurysms. In TM McGloughlin, editor, *Biomechanics and Mechanobiology of Aneurysms*. Springer, Berlin, 2011.

[44] P Mortier, GA Holzapfel, M De Beule, D Van Loo, Y Taeymans, P Segers, P Verdonck, and B Verhegghe. A novel simulation strategy for stent insertion and deployment in curved coronary bifurcations: Comparison of three drug-eluting stents. *Annals of Biomedical Engineering*, 38(1):88–99, 2010.

[45] M Nichols, N Townsend, R Luengo-Fernandez, J Leal, A Gray, P Scarborough, and M Rayner. *European Cardiovascular Disease Statistics 2012*. European Heart Network, Brussels, European Society of Cardiology, 2012.

[46] SJ Peterson and RJ Okamoto. Effect of residual stress and heterogeneity on circumferential stress in the arterial wall. *Journal of Biomechanical Engineering*, 122(4):454–456, 2000.

[47] S Polzer, J Bursa, TC Gasser, R Staffa, and R Vlachovsky. A numerical implementation to predict residual strains from the homogeneous stress hypothesis with application to abdominal aortic aneurysms. *Annals of Biomedical Engineering*. In press.

[48] MA Puso and J Solberg. A stabilized nodally integrated tetrahedral. *International Journal for Numerical Methods in Engineering*, 67(6):841–867, 2006.

[49] A Rachev and SE Greenwald. Residual strains in conduit arteries. *Journal of Biomechanics*, 36(5):661–670, 2003.

[50] ML Raghavan, S Trivedi, A Nagaraj, DD McPherson, and KB Chandran. Three-dimensional finite element analysis of residual stress in arteries. *Annals of Biomedical Engineering*, 32(2):257–263, 2004.

[51] C Reeps, A Maier, J Pelisek, F Härtl, V Grabher-Meier, WA Wall, M Essler, H-H Eckstein, and MW Gee. Measuring and modeling patient-specific distributions of material properties in abdominal aortic aneurysm wall. *Biomechanics and Modeling in Mechanobiology*. In press.

[52] JAG Rhodin. Architecture of the vessel wall. In DF Bohr, AD Somlyo, and HV Sparks, Jr, editors, *Handbook of Physiology. The Cardiovascular System*, pages 1–31. American Physiological Society, Bethesda, 1980.

[53] JF Rodríguez, G Martufi, M Doblaré, and EA Finol. The effect of material model formulation in the stress analysis of abdominal aortic aneurysms. *Annals of Biomedical Engineering*, 37(11):2218–2221, 2009.

[54] JF Rodríguez, C Ruiz, M Doblaré, and GA Holzapfel. Mechanical stresses in abdominal aortic aneurysms: Influence of diameter, asymmetry, and material anisotropy. *Journal of Biomechanical Engineering*, 130(2):021023, 2008.

[55] VL Roger, AS Go, DM Lloyd-Jones, EJ Benjamin, JD Berry, WB Borden, DM Bravata, S Dai, ES Ford, CS Fox, HJ Fullerton, C Gillespie, SM Hailpern, JA Heit, VJ Howard, BM Kissela, SJ Kittner, DT Lackland, JH Lichtman, LD Lisabeth, DM Makuc, GM Marcus, A Marelli, DB Matchar, CS Moy, D Mozaffarian, ME Mussolino, G Nichol, NP Paynter, EZ Soliman, PD Sorlie, N Sotoodehnia, TN Turan, SS Virani, ND Wong, D Woo, and MB Turner; on behalf of the American Heart Association Statistics Committee and Stroke Statistics Subcommittee. Executive summary: Heart disease and stroke statistics - 2012 Update: A report from the American Heart Association. *Circulation*, 125(1):188–197, 2012.

[56] N Sakalihasan, R Limet, and OD Defawe. Abdominal aortic aneurysm. *Lancet*, 365(9470):1577–1589, 2005.

[57] AJ Schriefl, H Wolinski, P Regitnig, SD Kohlwein, and GA Holzapfel. An automated approach for three-dimensional quantification of fibrillar structures in optically cleared soft biological tissues. *Journal of the Royal Society Interface*, 10(80):20120760, 2012.

[58] AJ Schriefl, G Zeindlinger, DM Pierce, P Regitnig, and GA Holzapfel. Determination of the layer-specific distributed collagen fibre orientations in human thoracic and abdominal aortas and common iliac arteries. *Journal of the Royal Society Interface*, 9(71):1275–1286, 2012.

[59] L Speelman, EMH Bosboom, GWH Schurink, J Buth, M Breeuwer, MJ Jacobs, and FN van de Vosse. Initial stress and nonlinear material behavior in patient-specific AAA wall stress analysis. *Journal of Biomechanics*, 42(11):1713–1719, 2009.

[60] HC Stary, DH Blankenhorn, AB Chandler, S Glagov, W Insull, Jr, M Richardson, ME Rosenfeld, SA Schaffer, CJ Schwartz, WD Wagner, and RW Wissler. A definition of the intima of human arteries and of its atherosclerosis-prone regions. A report from the Committee on Vascular Lesions of the Council on Arteriosclerosis, American Heart Association. *Circulation*, 85(1):391–405, 1992.

[61] CJ Stimpson, CD Ernst, P Knupp, PP Pébay, and D Thompson. *The Verdict Geometric Quality Library*. Sandia National Laboratories, 2007.

[62] J Tarjuelo-Gutierrez, B Rodriguez-Vila, DM Pierce, TE Fastl, P Verbrugghe, I Fourneau, G Maleux, P Herijgers, GA Holzapfel, and EJ Gomez. High-quality conforming hexahedral meshes of abdominal aortic aneurysms including their intraluminal thrombi. Submitted.

[63] J Tong, T Cohnert, P Regitnig, and GA Holzapfel. Effects of age on the elastic properties of the intraluminal thrombus and the thrombus-covered wall in abdominal aortic aneurysms: Biaxial extension behaviour and material modelling. *European Journal of Vascular and Endovascular Surgery*, 42(2):207–219, 2011.

[64] RN Vaishnav and J Vossoughi. Estimation of residual strains in aortic segments. In CW Hall, editor, *Biomedical Engineering II: Recent Developments*, pages 330–333. Pergamon Press, New York, 1983.

[65] JP Vande Geest, MS Sacks, and DA Vorp. The effects of aneurysm on the biaxial mechanical behavior of human abdominal aorta. *Journal of Biomechanics*, 39(7):1324–1334, 2006.

[66] DA Vorp. Biomechanics of abdominal aortic aneurysm. *Journal of Biomechanics*, 40(9):1887–1902, 2007.

[67] Y Wang and QJ Wang. The prevalence of prehypertension and hypertension among US adults according to the new joint national committee guidelines: New challenges of the old problem. *Archives of Internal Medicine*, 164(19):2126–2134, 2004.

[68] H Weisbecker, DM Pierce, and GA Holzapfel. A generalized prestressing algorithm for finite element simulations of pre-loaded geometries with application to the aorta. Submitted.

[69] H Weisbecker, DM Pierce, P Regitnig, and GA Holzapfel. Layer-specific damage experiments and modeling of human thoracic and abdominal aortas with non-atherosclerotic intimal thickening. *Journal of the Mechanical Behavior of Biomedical Materials*, 12:93–106, 2012.

[70] H Weisbecker, DM Pierce, B Rodriguez-Vila, EJ Gomez, and GA Holzapfel. A computational framework for patient-specific modeling of human arteries considering initial stresses and supra-physiological loads. Submitted.

[71] S Ylä-Herttuala, JF Bentzon, M Daemen, E Falk, HM Garcia-Garcia, J Herrmann, I Hoefer, JW Jukema, R Krams, BR Kwak, N Marx, M Naruszewicz, A Newby, G Pasterkamp, PWJC Serruys, J Waltenberger, C Weber, and L Tokgözoglu. Stabilisation of atherosclerotic plaques. Position paper of the European Society of Cardiology (ESC) Working Group on atherosclerosis and vascular biology. *Thrombosis and Haemostasis*, 106(1):1–19, 2011.

[72] PA Yushkevich, J Piven, HC Hazlett, RG Smith, S Ho, JC Gee, and G Gerig. User-guided 3D active contour segmentation of anatomical structures: Significantly improved efficiency and reliability. *NeuroImage*, 31(3):1116–1128, 2006.

[73] OC Zienkiewicz, RL Taylor, and JZ Zhu. *The Finite Element Method: Its Basis and Fundamentals*. Butterworth-Heinemann, Oxford, 2005.